MICROCOPY RESOLUTION TEST CHART

NATIONAL BUREAU OF STANDARDS-1963-A

An Experimental Investigation of Appendage-Flat Plate Junction Flow Volume I: Description

by
Stuart C. Dickinson

DTIC
ELECTE
JUN 1 2 1987
E

87 6 10   072

COMMANDER   00

TECHNICAL DIRECTOR   01

OFFICER IN CHARGE CARDEROCK 05	OFFICER IN CHARGE 04 ANNAPOLIS
SHIP SYSTEMS INTEGRATION DEPARTMENT 12	PROPULSION AND AUXILIARY 27 SYSTEMS DEPARTMENT
SHIP PERFORMANCE DEPARTMENT 15	SHIP MATERIALS ENGINEERING 28 DEPARTMENT
AVIATION AND SURFACE EFFECTS DEPARTMENT 16	
STRUCTURES DEPARTMENT 17	
COMPUTATION, MATHEMATICS & LOGISTICS DEPARTMENT 18	
SHIP ACOUSTICS DEPARTMENT 19	
CENTRAL INSTRUMENTATION DEPARTMENT 29	

AD-A181386

REPORT DOCUMENTATION PAGE

1a. REPORT SECURITY CLASSIFICATION Unclassified		1b. RESTRICTIVE MARKINGS		
2a. SECURITY CLASSIFICATION AUTHORITY		3 DISTRIBUTION/AVAILABILITY OF REPORT APPROVED FOR PUBLIC RELEASE: DISTRIBUTION IS UNLIMITED.		
2b. DECLASSIFICATION/DOWNGRADING SCHEDULE				
4. PERFORMING ORGANIZATION REPORT NUMBER(S) DTNSRDC-86/051		5. MONITORING ORGANIZATION REPORT NUMBER(S)		
6a. NAME OF PERFORMING ORGANIZATION David W. Taylor Naval Ship R&D Center	6b OFFICE SYMBOL (If applicable) Code 1542	7a. NAME OF MONITORING ORGANIZATION		
6c. ADDRESS (City, State, and ZIP Code) Bethesda, MD 20084-5000		7b. ADDRESS (City, State, and ZIP Code)		
8a. NAME OF FUNDING/SPONSORING ORGANIZATION Naval Sea Systems Command	8b. OFFICE SYMBOL (If applicable) Code 05R24	9. PROCUREMENT INSTRUMENT IDENTIFICATION NUMBER		
8c. ADDRESS (City, State, and ZIP Code) Washington, DC 20362		10 SOURCE OF FUNDING NUMBERS		

10 SOURCE OF FUNDING NUMBERS			
PROGRAM ELEMENT NO 61153N	PROJECT NO	TASK NO SR0230101	WORK UNIT ACCESSION NO DN178061

11 TITLE (Include Security Classification)
AN EXPERIMENTAL INVESTIGATION OF APPENDAGE-FLAT PLATE JUNCTION FLOW.
VOLUME I: DESCRIPTION

12 PERSONAL AUTHOR(S)
Dickinson, Stuart C.

13a. TYPE OF REPORT Final	13b. TIME COVERED FROM _____ TO _____	14 DATE OF REPORT (Year, Month, Day) 1986 December	15 PAGE COUNT 67

16 SUPPLEMENTARY NOTATION

17	COSATI CODES		18 SUBJECT TERMS (Continue on reverse if necessary and identify by block number)
FIELD	GROUP	SUB-GROUP	Separated flow; Flow visualization; Turbulence; Hot-film measurements Three-dimensional flow

19 ABSTRACT (Continue on reverse if necessary and identify by block number)

A horseshoe root vortex secondary flow forms at the junction of a flat plate and an appendage, creating a three-dimensional, separated flow. Flow visualizations, pressure measurements on the flat plate, and three-dimensional mean and fluctuating velocity measurements were made for two appendage shapes at zero angle of attack with a turbulent incoming boundary layer. The radius of curvature of the leading edge affects the strength of the secondary vortex flow. The vorticity is close to the wall, on the order of the momentum thickness of the incoming boundary laeyer, and has a flattened shape. The vortex breaks down and the vorticity is conserved as shear layers alongside of and in the wake of the appendage.

Keywords!

20 DISTRIBUTION/AVAILABILITY OF ABSTRACT ☐ UNCLASSIFIED/UNLIMITED ☒ SAME AS RPT ☐ DTIC USERS		21 ABSTRACT SECURITY CLASSIFICATION Unclassified	
22a NAME OF RESPONSIBLE INDIVIDUAL Thomas T. Huang		22b TELEPHONE (Include Area Code) (301) 227-1325	22c OFFICE SYMBOL Code 1542

DD FORM 1473, 84 MAR 83 APR edition may be used until exhausted
All other editions are obsolete

CONTENTS
VOLUME I

iii

CONTENTS (Continued)
VOLUME I

VOLUME II
(Report DTNSRDC-86/052)

(The appendixes are on microfiche at the end of Volume II.)

Appendix A. Data Base for Inflow Plane at x/c = −0.75

Appendix B. Data Base for Appendage Plane at x/c = 0.18

Appendix C. Data Base for Appendage Plane at x/c = 0.64

Appendix D. Data Base for Appendage Plane at x/c = 0.75

Appendix E. Data Base for Appendage Plane at x/c = 0.93

Appendix F. Data Base for Wake Plane at x/c = 1.05

Appendix G. Data Base for Wake Plane at x/c = 1.50

FIGURES

FIGURES (Continued)

ABSTRACT

A horseshoe root vortex secondary flow forms at the junction of a flat plate and an appendage, creating a three-dimensional, separated flow. Flow visualizations, pressure measurements on the flat plate, and three-dimensional mean and fluctuating velocity measurements were made for two appendage shapes at zero angle of attack with a turbulent incoming boundary layer. The radius of curvature of the leading edge affects the strength of the secondary vortex flow. The vorticity is close to the wall, on the order of the momentum thickness of the incoming boundary layer, and has a flattened shape. The vortex breaks down and the vorticity is conserved as shear layers alongside of and in the wake of the appendage.

ADMINISTRATIVE INFORMATION

ORGANIZATION

This report is organized into two volumes. Volume I can be read independently of Volume II. Volume II is designed to be used in conjunction with Volume I. Volume I contains a literature survey, a description of the experimental arrangement, a presentation of the analyzed data, and a discussion of the results. All conclusions are drawn in this volume. Volume II provides the researcher with a detailed data base. Volume II presents the data for the flow around an elliptical nose hybrid appendage. A complete listing of the data from each measurement location is provided, as well as the "raw" plots of the data. The data contained in Volume II will be available from the author on digital magnetic tape. Volume II will be valuable to numerical modelers as a test case for appendage junction predictions.

INTRODUCTION

The junction between a body and an appendage is a simple configuration with a complicated flow. Such configurations are found in many areas of fluid engineering including the wing-fuselage junction of aircraft, the appendage-hull junction of ships and submarines, and the blade-end wall junction of turbomachinery. A "horseshoe root" vortex secondary flow forms in the junction region and affects the drag, lift, and heat transfer. The secondary flow persists downstream causing effects in the wake. The work presented here is part of an effort to understand and document an idealized appendage-body junction flow. The results provide valuable assistance in the development of numerical flow prediction codes for naval designs.

1

In a simple description of the secondary flow formation, the vorticity present in the oncoming boundary layer is slowed down by the pressure gradients near the leading edge of the appendage. Away from the appendage, the flow continues undisturbed so the vorticity is wrapped around the appendage. A concentration and a turning of the oncoming cross-flow vorticity into streamwise vorticity occurs. The vortex lines can not be broken by the appendage so they trail downstream with the flow. The result is a horseshoe root vortex secondary flow with three-dimensional separations and attachments.

The horseshoe root vortex secondary flow forms in both laminar and turbulent flows. One does not necessarily expect the two flows to be similar in detail. This report deals with the turbulent case where the oncoming body boundary layer is fully developed turbulent boundary layer. The flow has been simplified as much as possible. The body chosen is a zero-pressure-gradient flat plate, and the appendage is semi-infinite with a zero degree angle of attack. The physical model used one wall of a wind tunnel as the body and an appendage spanning the test section. Blockage is present in the wind tunnel. The calculated blockage for a potential flow is 3% at the appendage location.

For the purposes of this report, the appendage-flat plate flow is divided into three main regions (see Fig. 1). These regions are conceptual and do not have rigorous boundaries. The first region is the upstream inflow region where the flow has not responded to the presence of the appendage. This flow is characterized by a two-dimensional, zero pressure gradient, turbulent boundary layer. The second region is the appendage region. This region includes all the strong pressure gradients and the generation of secondary flows associated with the presence of the appendage. The second region is further divided into three subregions: the leading edge, alongside, and the trailing edge. The third region is downstream of the appendage and is called the wake. The wake is subdivided into the near and far wakes. The near wake starts at the trailing edge and includes the area actively affected by the appendage. This would be the region where appendage generated pressure gradients exist. The far wake is downstream of the near wake and is the region where no new secondary flows are forming; however, the previously generated junction flow is present and decaying.

The measurements presented in this report are oil film and oil dot flow visualizations, static pressure measurements on the flat plate, and hot-film anemometer measurements of mean and fluctuating velocities upstream, alongside, and in the wake of the appendage. The flow visualizations and pressure measurements were conducted for a National Advisory Committee for Aeronautics (NACA) 0020 shape appendage and an elliptical nose hybrid appendage. The oncoming boundary-layer thicknesses were used for each shape. The hot-film data is for one boundary-layer thickness, using the elliptical nose appendage.

LITERATURE REVIEW

This review is intended to provide an overview of the subject and a review of current publications, it is not intended to be exhaustive. Two documents with good

2

literature reviews are Peake and Tobak[1] and Sung.[2] This section is written in three parts with the publications discussed according to type: *experimental, analytical, and numerical.*

Experimental

The bulk of the published work on appendage body junctions consists of experimental investigations of various geometries. It is convenient to break the appendage geometry down into three broad groups: cylinders, infinite chord wings, and streamlined foils. Two types of flows are possible—laminar and turbulent. Only incompressible turbulent flows will be emphasized in this review.

An early piece of significant research was performed by Love.[3] He investigated the effect of the leading edge shape and concluded that the curvature of the leading edge is instrumental in determining the strength of the secondary flow. This conclusion has not been significantly improved since then; although, some of the details of the flow have been clarified. Even though the junction flow around a cylinder has a simple geometry, the kinematics are complicated by separation on the lee side. Several investigators have studied this flow including Belik[4] and Baker.[5]

Several investigators have studied the infinite chord wing. Shabaka,[6] and Shabaka and Bradshaw[7] performed an exhaustive investigation of this geometry using an uncambered constant thickness wing at zero degree angle of attack. The leading edge was a 1:6 ellipse. Shabaka performed oil film flow visualization, static pressure measurements on the body (a zero pressure gradient flat plate), Pitot and Preston tube measurements, and three-dimensional hot-wire measurements of the mean velocities and Reynolds stresses. The measurements were performed in the constant thickness region alongside the appendage. This work documents the downstream development of the secondary flow. Shabaka found regions of negative shear stresses in the corner. One of his conclusions is that eddy viscosity and mixing length models are not suitable for this type of flow. Oguz[8] investigated a similar wing body junction flow with a 1:1.5 semielliptic leading edge. This blunter leading edge produced stronger cross-flow velocities in the junction region. Oguz measured the flow alongside the wing. Kubendran,[9] and McMahon et al.[10,11] used the same body as Oguz but performed hot-wire measurements in the reversed flow region at the leading edge. In the plane of symmetry Kubendran measured upstream moving fluid near the body.

Cylindrical and infinite-chord appendages are good fundamental shapes, but they are not realistic aerodynamic or hydrodynamic shapes. Thus, several investigators have examined the flow around streamlined foils. In general, these foils have been idealized; however, the physics of the flow around around naval appendages was maintained. Pierce has had an ongoing program of research on the flow around a cylindrical leading edge foil. Pierce and McAllister[12,13] studied the turbulent boundary layer outside the separated region including direct wall shear stress measurements. Menna and Pierce[14] made hot-wire measurements, including Reynolds stresses, in the same region. Harsh and Pierce,[15] using a five-hole Pitot tube, measured the flow in the plane of symmetry ahead of the foil, and in cross flow

planes at positions of 43% and 100% chord. This work included the reversed flow in the leading edge region. Pierce, Harsh, and Menna[16] summarize the last two references. Dickinson[17] examined the flow around an elliptical nose (1:1.5) NACA tail appendage (the same model used for this report) using time dependent flow visualization techniques and laser doppler anemometry. Velocity measurements were made near the reversed flow region ahead of the foil. The author concluded that the vortex was flattened and of small extent in the Y direction (away from the flat plate). Rood[18] examined the large-scale, time-dependent flow around several elliptical nose foils. He identified several regions where tubulence with new frequency scales was created. Rood and Keller[19] showed that the low frequency velocity fluctuations were either in or out of phase, allowing the use of two point velocity correlations to identify the legs of the vortex flow downstream. Rood[20] investigated the spatial extent of the vortex legs when the appendage was at a small angle of attack. Rood[21] also examined the effect of leading edge radius, and Rood and Anthony,[22] the effect of tail geometry; both studies were for a small angle of attack. Hasan, Casarella, and Rood[23] investigated the fluctuating pressures on the wall in the junction region of an appendage with zero angle of attack.

Analytical

The useful analytical work on wing-body junctions has been in the area of topology. This analysis defines the types of flow possible in three-dimensional separated regions. Lighthill[24] describes nodal points of attachment and separation, saddle points, and other topographic features. These features are examined as they apply to skin-friction lines (oil film flow visualizations) and vortex lines. Hunt et al.[25] examine the relationships between topography and flow visualization for bluff objects on a flat plate. Perry and Hornung[26] examine vortex skeletons and the resulting wall streamlines. They apply the results to an electromagnetic analogy of flow with wall slip.

Numerical

Numerical solution of the flow past a wing-body junction has received little attention in the past; this is due in large part to the complexity of the flow field, which may involve separation and large regions of reversed flow.

Attempts have been made to determine the flow in the region between the leading and trailing edge by Gorski et al.,[27] Kline et al.,[28] and Ilegbusi.[29] These calculations, however, assume the flow to be parabolic, and are started downstream of the wing leading edge using experimental data as the initial conditions. As such, they are incapable of predicting the development of the horseshoe root vortex at the wing leading edge.

Numerical simulation of the flow in the wing leading edge area including the separated region has been conducted using several methods, none of which have been entirely satisfactory. Smith and Gajjar[30] use triple deck boundary layer theory to analyze the three-dimensional laminar flow past a junction formed by a thin wing protruding from a locally flat body surface, with the Reynolds number taken to be

large. The results show good quantitative agreement with experimental data, although it is not clear how this technique could be generalized to more realistic bluff wing-body configurations.

Kaul et al.,[31] in a more generalized approach, simulated the incompressible low Reynolds number laminar flow around a cylinder-end wall junction by solving the incompressible Navier Stokes equations in three dimensions. The equations, cast in generalized curvilinear coordinates, are solved in time as a hyperbolic system by adding a pressure term in the continuity equation and are marched to a steady state. The numerical results reveal the formation of the horseshoe root vortex and various physical quantities associated with the saddle point of separation. Computational and experimental results are generally consistent. At DTNSRDC, R.W. Burke is currently using this model to simulate the ellipitcal nose appendage junction flow documented in this report.

The discussion thus far has been limited to incompressible flows, which are the main area of interest for naval ship applications. In addition, however, wing-body juncture regions occur in many configurations of practical importance involving compressible, supersonic flow. Briley and McDonald[32] solved the compressible Navier Stokes equations for a laminar horseshoe root vortex flow created by the intersection of an elliptical strut and a flat plate. The calculations were carried out on a coarse mesh, extending over a small region around the leading edge. The outflow boundary was placed at about midchord of the strut, eliminating simulation in the trailing edge and wake regions.

Hung and MacCormack[33] and Hung and Buning[34] have solved the complete compressible Navier Stokes equations for supersonic flow over a three-dimensional compression corner. A simple eddy viscosity model, based on the Baldwin-Lomax scheme,[35] is used to parameterize the turbulent shear stresses. The numerical results show generally good agreement with experimental data. As far as the author is aware, these are the only published attempts at simulation of turbulent viscous flow in a wing-body junction.

DESCRIPTION OF THE EXPERIMENT

MODEL

The Wind Tunnel

The experiments described in this report were all performed in the DTNSRDC Low-Turbulence Wind Tunnel (LTWT). The test section is 0.61-m wide (2 ft), 1.22-m high (4 ft), and 4.57-m long (15 ft). The test section velocity varies up to 40 m/s (130 ft/s) with a free stream rms turbulence level less than 0.2%. Scottron and Shaffer[36] give the details of the tunnel design. Access to the tunnel was either through the top of the tunnel or through existing static pressure taps. The top of the tunnel was used as the flat plate of the appendage junction. The side walls of the LTWT are flexible, allowing the creation of pressure gradients; however, for this investigation the tunnel walls were parallel and straight. Any pressure gradients were a result of either boundary-layer growth on the walls or the presence of the model. Corner fillets were added to the junction between the top and the side walls of the tunnel to reduce the

5

corner secondary flows (see Fig. 2). This improved the two dimensionality of the flat plate boundary layer.

Appendage

Two types of appendages were used during this investigation. Both models were semi-infinite, spanning the height of the wind tunnel.

The first appendage tested had a NACA 0020 profile with a chord of 30.48 cm (12 in.) and a thickness of 6.1 cm (2.4 in.) as shown in Fig. 3. Flow visualization and pressure measurements were made for this model and will be presented later in this report. Preliminary three-dimensional velocity measurements were made with cylindrical hot-film probes and revealed that the cross-stream flows for this appendage were too weak to resolve accurately. A new appendage with stronger cross-stream flow in the junction region was needed.

A elliptical nose appendage was designed consisting of a 1.5:1 elliptical nose and a NACA 0020 tail joined at maximum thickness locations. The resulting appendage has a chord of 25.9 cm (10.2 in.) and a thickness of 6.1 cm (2.4 in.) as shown in Fig. 3. The thickness was the same for both appendages to maintain a constant area blockage in the wind tunnel. The NACA tail was chosen because the flow visualization on the NACA 0020 foil showed no separation on the flat plate in the trailing edge region. Offsets of both appendages can be found in Table 1. Both appendages were fitted with 0.013-in. (0.33-mm) trip wires at an x/c location of 0.05. A 1.5:1 elliptical leading edge was chosen because this shape had been investigated by Oguz[8] and creates up to a 10% cross-flow velocity alongside a constant thickness body. The bulk of the data in this report was taken in the flow around the elliptical nose appendage; however, data taken in the NACA 0020 flow is included as a comparison between the effects of leading edge radii.

Coordinate System

The coordinate system used in this research is right-handed cartesian. The origin is located at the junction of the appendage leading edge and the flat plate. The x-axis is the junction of the appendage chord and the flat plate (positive downstream), with the y-axis along the span of the appendage (positive away from the flat plate), and the z-axis in the cross stream direction (see Fig. 4). The velocity components u, v, and w represent the fluid velocities along the x, y, and z axes, respectively.

EQUIPMENT

Flow Visualization

Extensive flow visualization was performed during the course of this work. Two techniques were successful: oil films and oil dots. Both techniques used the same type of mixtures consisting of an SAE 30 motor oil vehicle with a carbon black pigment and a small amount of oleic acid as a dispersant. The actual viscosity of the mixture was determined by the amount of pigment used and was determined by trial and error for each velocity. During a series of visualizations, a single batch was used, reducing variation. The oil films were applied with a paint brush and the oil dots with a screw actuated hypodermic.

6

The flow visualization was performed on the flat plate (tunnel top) which is constructed out of a clear acrylic sheet. Two problems were encountered. First, the acrylic sheet absorbs oil, thus reducing the surface tension forces on the oil; this is an advantage. However, the surface must be "aged" by repeated application of oil for a week. Second, static electricity can build up on the plastic (especially from polishing) and cause erratic movement of oil drops. This was prevented by using a commercially available conductive spray (for clothes). A complete description of the flow visualization techniques can be found in Dickinson.[17]

Reference Pitot Tubes

Pressure and thermal transducers were used to measure velocity. Two pitot tubes served as references, one for measuring the free-stream velocity u_{ref} and one for calibration. The reference pitot tube was installed 8.55 in. (21.7 cm) ahead of the appendage and in the free-stream flow (Fig. 5). The calibration pitot tube was used to calibrate the hot-film probes. It was located in the measurement plane and at y = 7.0 in. (17.78 cm) and z = 7.5 in. (19.05 cm). The total and static pressures from the pitot tubes lead to a Datametrics 572D-10T-2E3-V3X Barocell Differential Pressure Sensor and Datametrics 1174-2C Barocell Electric Manometer. The manometer displayed the pressure and provided an analog output with one torr equal to one volt. The analog output was connected to channel zero of the Analog to Digital Converter (A/D). Using an air density table, the operator determined the density by measuring the temperature, relative humidity, and barometric pressure. Then, given the air density, the computer calculated the pitot velocity.

Static Pressure Taps

Static pressure measurements were made on the flat plate in the junction region. One hundred and forty-eight static pressure taps (0.035 in. (0.089 cm) in diameter) were drilled in a plexiglass window. A scanvalve system was used to connect each pressure tap to the Barocell Manometer. The static pressure from the reference pitot tube ahead of the appendage was defined as the zero pressure level.

Positioning

Velocity measurements were made with a hot-film sensor mounted on a probe body. This probe body was clamped to a strut which passed through a slit in the plexiglass ceiling of the test section. The strut was attached to a stepper motor traverse apparatus which moved in the y-direction. The traverse was mounted on a lathe bed which could move in the z-direction. For a diagram of this apparatus, see Fig. 6. Movement in the x-direction was achieved by sliding the probe in the strut and clamping it in the desired position. To collect data, a measurement plane was selected (e.g., x = 7.65 in.). The probe was positioned in the strut and could then be moved anywhere in the yz-plane.

Because of the nature of the flow, an uneven grid of data points was used (see Fig. 7). Away from the appendage, there is little change in velocity with change in position. However, in the turbulent boundary layers, small changes in position

produce large changes in velocity. Thus, near the plate and the appendage, data points are fairly dense while out in free-stream they are sparse.

To facilitate data collection, the traverse was equipped with R.I. Controls 7100-12 Displacement Transducers providing a voltage output which was linear with position. These potentiometer type transducers were mounted on both the strut and the traverse to give an output for both the y- and z-positions. A Tektronix PS 503A Dual Power Supply provided a -7.5 and $+7.5$ voltage across each 1000 ohm potentiometer. The output of each transducer was then displayed on Tektronix DM 501 multimeters and was read by the computer through channels 5 and 6 of the A/D converter. By performing a least squares linear regression, the slopes (in./V) and intercepts (in.) were found and entered in the computer. The y-position constants were also entered in a Fluke 8500A multimeter to give a direct readout o the current y-position to the operator. The x-position was entered directly in channel 4 of the A/D as an arbitrary voltage. By giving the computer the appropriate constants, the correct x-position in inches was determined.

To simplify data collection, the traverse was designed with a Superior Electric SLO-SYN stepping motor which was controlled by a SLO-SYN Preset Indexer. When taking data, the operator set the appropriate number of steps (400 steps/in.) and directed the motor to move the probe to the next y-position. As the desired accuracy for positioning was 0.01 in., the allowable error was plus or minus 0.005 in., two steps of the motor.

Hot-Film Anemometry

The mean and fluctuating three-dimensional velocity data were measured with cylindrical hot-film probes in an "X" configuration. With the two-dimensional probes, only two of the three velocity components, u, v, and w could be measured simultaneously. To get the third component, two measurements at each data location were made—one with the films vertical to find u and v and one with the films horizontal to find u and w.

The small, nonlinear signals from the hot films were conditioned. First the voltage signals were produced using TSI 1241-20 (0.002-in. diameter film) probes and 1050 Constant Temperature Anemometers. These anemometers used TSI 1323 Temperature Compensating Resistors to eliminate some errors caused by fluctuating air temperature in the wind tunnel. Each signal was then linearized with TSI 1052 fourth order polynomial linearizers. Finally, TSI 1057 Signal Conditioners were used to suppress the signals by -5.0 V (to match A/D input levels) and to filter out noise above 20 kHz. The signal output from the 1057's was linear with velocity and varied between -5.0 and 5.0 V.

In order to enable the operator to visualize the fluctuating velocities in the boundary layers, and to ensure that the hot-film sensors are operating properly, the linearized signals were observed on a Tektronix SC 502 oscilloscope. The computer then read the signals through channels 1 and 2 of the A/D. Before they could be used, however, the hot-films were calibrated using the calibration pitot tube shown in Fig. 5. This pitot tube was at the same x location as the hot film and in the free-

8

stream flow at y = 7.0, z = 7.5 in. At this calibration location it was assumed that the cross-flow velocities were zero. By switching valves, this calibration pitot tube pressure was processed through the Barocell system and was read through channel 0 of the A/D.

The hot-film probe was calibrated by placing it at y = 6.0 in. and z = 7.5 in., just above the pitot tube. The computer calibration program sets the u velocity of the hot film equal to that which the pitot tube measures and the cross-stream velocity (v or w) equal to zero. By taking data at different tunnel speeds, the computer then ran a linear regression routine to find the slopes and intercepts for each channel. The hot-film voltages were then converted into velocities. The sum of the voltages was proportional to u and their difference was proportional to v or w. At any time during data collection, the operator could bring the probe back to the calibration position, switch to the calibration pitot tube, and check the velocities. The u velocity calibration was maintained within 1% (0.3 m/s) of the pitot tube velocity and the cross-flow velocity was maintained to be zero within 1% of free stream (0.3 m/s). Typical calibration drift during data collection was less than 0.5%.

DATA COLLECTION

Data collection for this project was automated with a microcomputer. A Digital PDP-1123 processor was used with a 10 Mb Winchester hard disc. A Data Translations 2782-SE-A analog to digital converter was used to interface the analog instrumentation to the computer. A menu driven software package was created to collect the data, perform the initial data processing, and create a data file structure. Details of the software package may be found in Middlekauff and Dickinson.[37]

At each measurement location, the computer determined the position from the potentiometers and then took 5000 readings, each reading spaced by 20 milliseconds, of the reference pitot tube and the two hot-film signals. The mean velocities were then computed. Going through the hot-film data again, the mean square of the fluctuating components and the cross terms were determined (i.e., mean square u, mean square v, and uv). Finally, the position coordinates, the reference velocity, the two mean velocities, the two root mean squared velocities, and the cross velocity were stored in a data file. Fig. 8 is a block diagram of the data collection system.

ACCURACY

Two corrections were made to the raw hot-film data. One correction involved a calibration of the angular sensitivity of the X film probes. The probes were calibrated in free stream for both yaw (in the plane of the X) and pitch. The effect of yaw was removed by using a calibration procedure. The effect of pitch was small for the range of flow angles encountered in this investigation, so the difference was included in the accuracy calculation. The effect of shear across the plane of the X film probe was significant (for the cross-flow velocity) in certain areas of the flow. This effect was removed by post processing the data to determine the local shear in the u velocity and calculating the shear-induced bias caused by the separation of the cylindrical film sensors.

The accuracy of the investigation was determined after an extensive error analysis. The mean velocities are accurate within plus or minus 2.5% of the free-stream velocity with a 95% confidence level. This accuracy is a worst case calculation for regions of high shear and includes the effect of positioning uncertainty. In regions of low shear the accuracy is estimated to be plus or minus 1.5%.

DATA

This section presents the data obtained during the course of this experimental investigation. The results of both the NACA 0020 and the ellipitcal nose appendages are presented. The NACA appendage was used for parametric studies of the effect of boundary-layer thickness and free-stream velocity. The elliptical nose appendage was investigated in detail for one set of parameters. In this volume of the report the results from the elliptical nose appendage have been reduced in order to highlight the effects of the secondary flow. Volume II of this report contains the "raw" data and plots of the elliptical nose appendage flow.

NACA 0020 APPENDAGE

Flow Visualization

Oil-film and oil-dot flow visualization was performed for the NACA 0020 appendage shape. The effects of parametric changes were investigated. These changes consisted of two incoming boundary-layer thicknesses (1.0 and 2.5 in.) and three free-stream velocities (23.5, 30.5, and 35.2 m/s). Figs. 9a-9c show sketches of the oil-film flow visualizations at three different speeds. There is no apparent change in the flow pattern with the two higher velocities (Figs. 9b-9c). The shear stress gradient line appears to change at the leading edge and move closer to the leading edge for the lowest speed case; however, this effect is due to a mismatch of the oil viscosity for the flow condition rather than a true effect.

Oil dots were also used to investigate the effect of free-stream velocity. Fig. 10 shows a sketch of the primary separation line and an attachment line as deduced from the oil dot traces for the intermediate velocity. The oil film and oil dot results agree reasonably well for the attachment line; however, the separation line varies somewhat. The oil film separation line is believed to be more accurate since there is some uncertainty in the determination of the separation from the weakly converging and quantized oil dot path lines. Figs. 11a-11c show the dot traces for the three free-stream velocities. No significant differences are seen between the results.

The effect of boundary-layer thickness was investigated using oil dots for the intermediate velocity. Fig. 11d shows the dot traces for the thin boundary layer. No significant differences are seen as a result off this thiner boundary layer.

Pressure Measurements

Static pressure measurements were made on the flat plate. The results for the NACA 0020 appendage at the medium velocity and thick boundary layer can be found in Fig. 12.

10

Velocity Measurements

Velocity measurements were made using "X" hot-film sensors at one measurement plane for the NACA 0020 appendage. This plane was located at the position of maximum thickness of the foil (x/c = 0.30). During this phase of the investigation it was discovered that the cross flow velocities (v, w) were weak. It was determined that the velocity to velocity uncertainty ratio was too small for the accuracy needed in an investigation designed in part to provide an accurate data base for comparison with numerical models. Thus the elliptical nose appendage was developed to increase the cross flow velocities.

ELLIPTICAL NOSE APPENDAGE

Flow Visualization

The flow around the elliptical nose appendage was visualized using time dependent oil-film techniques (see Dickinson[17] for details). Fig. 13 shows the flow pattern at various times T after the wind tunnel was rapidly brought up to speed.

Fig. 14 is a sketch of the fully developed oil-film pattern. It shows the primary separation line wrapped around the leading edge and trailing downstream. There is an inner line in the leading edge region which merges with the primary separation line near the one-half chord position. This line is interpreted not as a separation line but as a sharp demarkation between a high shear stress region inside and a much lower shear stress region outside. An attachment line is shown which is between a small inner counter-rotating vortex and the primary horseshoe root vortex. In the tail region, the vorticity induces a downwash, and "Y" shaped lines are observed.

Fig. 15 shows the oil dot results. This figure shows the local skin friction direction and gives a qualitative idea of the skin friction magnitude. Fig. 16 shows the same flow as visualized using an oil of wintergreen technique (Langston and Boyle[38]). All three flow visualization techniques show good agreement.

Pressure Measurements

Static pressure measurements were made on the flat plate. The results of the standard test case (u_{ref} = 30.5 m/s, δ = 2.5 in.) are shown in Fig. 17 (tabulation of these data may be found in Volume II). Figs. 18a-18c show the pressure coefficients measured at three different free-stream velocities, u_{ref} = 23.5, 30.5, and 35.2 m/s. It is obvious that free-stream velocity has no effect for this range of incoming velocity.

Velocity Measurements

Velocity measurements were made at seven different cross flow (x/c = constant) planes (see Fig. 19). The first plane was located upstream at x/c = -0.75. This plane represents the undisturbed inflow condition. Four measurement planes were located alongside the appendage. Plane x/c = 0.18 was located at the maximum thickness of the foil, and plane x/c = 0.64 duplicates a plane measured using an LDV in an earlier study (see Dickinson[17]). Plane x/c = 0.75 is the location used as a reference between investigators, and plane x/c = 0.93 was just upstream of the trailing edge. Two measurement planes were investigated in the wake of the

11

appendage. Plane x/c = 1.05 was just downstream of the trailing edge, complementing the previous plane, and was in the near wake. Plane x/c = 1.50 was in the wake as far downstream as the experimental setup allowed.

Measurements were made with "X" hot films and consisted of the three (u, v, w) mean velocities, root mean square (rms) of the three fluctuating velocities (u', v', w'), and two of the remaining Reynolds stresses (u'v', u'w'). These data were reduced and used to create graphs of the measured U velocity contours (Figs. 20a-20g), the measured cross-flow velocity vectors (Figs. 21a-21g), and the turbulent kinetic energy contours (Figs. 22a-22g).

DISCUSSION

PRESSURE

The main driving force behind the secondary flow around an appendage-flat plate junction is the pressure. Most of the pressure field is generated by the two-dimensional flow around the appendage away from the wall. This pressure field is modified somewhat by the secondary flow, but only to a "small" degree. A numerical calculation of the pressures due to a two-dimensional potential flow around an appendage was made using the "Airfoil" code.[39] This calculation included the presence of the wind tunnel walls as they existed in the experiment. Figs. 23 and 24 show the results for the NACA 0020 and elliptical nose appendages respectively. These calculations do not include the effects of boundary-layer development or wake blockage. Comparison of Figs. 23 with 12 (NACA 0020) and 24 with 17 shows good qualitative agreement. Some of the effects of the secondary flow, such as the low pressure core of the vortex, can be seen modifying the two-dimensional field in the experimental data.

As the flow approaches the appendage it experiences an adverse pressure gradient. This rising pressure slows the flow and diverts it around the leading edge. As the flow accelerates around the appendage, the pressure drops to a minimum near the area of maximum thickness of the appendage. Traveling downstream, the pressure rises again as the appendage thins. This region is the pressure recovery region of the foil. There is a high pressure region near the trailing edge as a result of the stagnation point there. Past the foil, the pressure relaxes to the ambient condition. The pressure variations are greatest near the appendage and drop off with distance. It is the interaction of the pressure gradients with the boundary layer that creates the secondary flow.

Two different foil shapes were used for this investigation. The difference between the foils was the leading edge shape ahead of the location of maximum thickness. The foils had identical shapes aft of the maximum thickness location. The NACA 0020 foil has smoother pressure variations near maximum thickness than the elliptical nose foil. The pressure gradients are steeper for the elliptical foil shape as expected from the blunter nose radius and greater thickness to chord ratio. As a result of the increased pressure gradients for the elliptical nose appendage, the secondary flows are expected to be greater than those associated with the NACA appendage. Since the pressure recovery geometry of the foils is identical, the pressure

12

fields in the aft regions of the foils are expected to be similar. These trends are seen in both the calculated pressure fields (Figs. 23 and 24) and the measured pressure fields (Figs. 12 and 17). The agreement between the calculated and measured pressures is qualitatively good; however, the magnitudes of the variations are less for the measured values. This effect is attributed to the three-dimensional nature of the real flow and pressure variations across the boundary layer.

The pressures were measured around the elliptical nose foil for three free-stream velocities (u_{ref} = 23.5, 30.5, and 35.2 m/s). The results are depicted in Figs. 18a-18c. No significant differences were found.

FLOW VISUALIZATION

Two primary types of flow visualizations were used for this investigation: oil film and oil dot. Both of these techniques are surface visualizations resulting from the flow of oil on the flat plate. In this work the primary force causing the movement of the oil was the shear stress of the air flow on the oil. The oil is a lagrangian marker and the oil flow streaks and traces are material lines at the wall. For steady flow, these lines should represent the wall streamlines. This flow, however, is not steady due to the turbulence. Whether the mean flow in the junction region is steady is not known, so caution must be used if the flow visualization results are to be interpreted as streamlines. The oil dot visualizations take several minutes to develop and the "completed" oil films nearly an hour to form, so they represent long time averages of the air flow. Despite this, the flow visualization reveals much useful information about the flow and is an important part of this investigation.

First the general features revealed by flow visualization of an appendage-flat plate junction will be discussed. After the general discussion, the differences and details of the individual visualizations will be described.

Figs. 13-15 will be used for the general description. Figs. 13f and 14 represent the completed oil-film visualization, and Fig. 15 represents the oil-dot visualization. The completed oil film photograph shows the primary features of a horseshoe root vortex. Ahead and alongside of but away from the appendage, one sees the oil streaks following the streamlines of the outer flow, basically unaffected by the secondary flow. From near the trailing edge aft, however, these streaks diverge in a manner much different than that seen in a two-dimensional flow. Along the centerline, ahead of the foil, one can see streaks that indicate a stagnation point type flow. The next feature closer to the appendage is the three-dimensional separation line. This line wraps around the appendage, trails off downstream, and is visualized by an accumulation of oil or pigment. A three-dimensional separation surface intersecting the flat plate creates the separation line. To the oil on the plate, the line is the location of a convergence, being unable to leave the wall, the oil accumulates. The accumulated oil eventually runs downstream along the separation line. It is important to remember that a three-dimensional separation line is characterized by zero shear stress normal to itself but that, in general, there exists shear along the line. This line is sketched as the primary separation line in Fig. 14. Between the

13

separation line and the leading edge, a second line can be seen. This is interpreted for the flows reported here to be a shear-stress gradient line. This line delineates a region of high shear near the foil from an area of lower shear outside. (In some flows, e.g., laminar, a line at this location is actually a secondary separation line.) The shear stress gradient line wraps around the leading edge and merges with the primary separation line alongside the foil. This line is also sketched in Fig. 14. There is evidence of a small counter rotating vortex in the corner of the appendage and the wall. This is indicated by the light scoured region around the leading edge (other visualization techniques highlight this feature more clearly). This vortex carries oil into the corner where it runs downstream and leaves the appendage in a "V" shaped pattern near the trailing edge. Inside this "V" can be seen a scoured region caused by the downwash of the wake of the appendage. The downwash is a result of the secondary flow pumping fluid down between the trailing legs. The "V" shaped line is sketched in Fig. 14.

Essential features of the flow highlighted by the oil dot visualization technique are seen in Fig. 15. A low shear stress region is seen near the leading edge separation. The forward moving reversed flow is clearly seen near the centerline, just forward of the appendage. As the flow accelerates around the nose, the vortex induces outward flow, and high shear stress is apparent. Alongside the appendage, the primary separation can be observed as a convergence of the streaklines. The small, inner, counter-rotating vortex is shown by the dots along the junction (rows 3-7) moving in toward the appendage and by the divergence of streaklines between the first and second sets of dots. Row 8 is the clearest example of the variation of shear stress in the cross-flow plane. Moving out from the appendage, the stress increases under the core of the vortex; it then reaches a maximum near the separation line and finally becomes constant in the outer region. In the wake region, the downwash is seen by the divergence of the streaks. Along the wake centerline the shear stress increases downstream as the wake velocity deficit (downwashed to the wall) is reduced.

Oil-film and oil-dot parametric studies were performed using the NACA 0020 appendage to investigate the effect of free-stream velocity and boundary-layer thickness on the secondary flow. Sketches of the oil film results are found in Figs. 9a-9c. These three figures represent a change in free-stream velocity or chord Reynolds number. The sketches show the location of the primary separation line, the shear stress gradient line, and the attachment line between the horseshoe vortex and the inner counter-rotating vortex. The shear stress gradient line in Fig. 9, obtained at the lowest speed (23.5 m/s), is distorted near the leading edge due to the viscosity of the oil. The same oil was used for Figs. 9a-9c to reduce experimental variation, but the oil was too viscous to respond properly in the low shear region ahead of the leading edge. Comparison of the three sketches shows no systematic variation due to velocity over the range tested. Fig. 10 is a sketch similar to Figs. 9a-9c; however, it is derived from an oil-dot visualization record (Fig. 11b). Using the methods discussed above in the general description, the locations of the primary separation and attachment lines were determined. The attachment line compares well with Fig. 9b, but some variation in the separation line is noted. This is not unexpected, however, since the oil dot technique is not an ideal method to determine accurately the location of weak (low convergence velocity) three-

dimensional separations. These visualizations were performed in the "thick" boundary layer (nominally 2.5 in. in the unperturbed flow upstream of the appendage).

Figs. 11a-11d are traces of oil-dot flow visualization around the NACA 0020 appendage. Figs. 11a-11c correspond to the same three free-stream velocities as Figs. 9a-9c in the thick boundary-layer. A "thin" (nominally 1.0 in. in the unperturbed flow upstream of the appendage) case was run for the intermediate velocity (30.5 m/s) and is shown in Fig. 11d. There is no effect on the flow visualization of changing either the boundary-layer thickness or the free-stream velocity.

Flow visualization was performed using the elliptical nose appendage. Parametric studies were made and showed no effect of free-stream velocity or boundary-layer thickness for the same variations as reported above for the NACA 0020 appendage. Extensive visualizations were performed for the standard test case parameters consisting of a free-stream velocity of 30.5 m/s and a nominal boundary-layer thickness of 2.5 in.

A method of time-dependent, oil-film flow visualization was used to yield additional information about the elliptical nose appendage junction region. Time-dependent flow visualization uses several views of the film as the flow pattern develops. During this process, the oil is moving at a speed and direction proportional to the local shear stress. Using photographs of the oil film at known time intervals, one can qualitatively determine the relative shear stresses. Fig. 13 (a-f) shows the flow pattern at various times T after the wind tunnel has rapidly been brought up to speed. Fig. 13a shows the film for T = 0. At T = 0.5 min (Fig. 13b), the oil has been removed from the area of highest shear stress. Fig. 13c (T = 1 min) shows the clear area moving upstream and lengthening around the foil. The oil has been scoured to the shear stress gradient line in Fig. 13d (T = 4 min) and is starting to move between this line and the primary separation. The outer region and the downwash area aft of the tail have also started to develop patterns. The clear lines close to and alongside the foil reveal the counter-rotating inner vortex with the oil collecting in the corner. In Fig. 13e (T = 10 min) the tail area pattern has developed and the leading edge region has "completed" or lost its oil. After 40 min, Fig. 13f shows the completed picture of the traditional method. Fig. 14 is a sketch of the completed oil-film visualization.

Oil-dot flow visualization is shown in Fig. 15. A complete description of this figure was given in the general discussion. A careful investigation was made in the trailing edge region to determine whether a reversed-flow separation exists there. No evidence was found to indicate that the oil ever moved in the upstream direction (near the trailing edge on the flat plate). An oil dot study also indicated that no two-dimensional separation existed on the foil near maximum thickness in the free-stream flow.

Comparisons between Figs. 14 and 15 show good agreement between these two techniques. A close examination was made of the leading edge region using the oil of wintergreen technique (Langston and Boyle[39]). A sketch of the results is seen in

Fig. 16. Streaklines cross the shear stress gradient line of Fig. 14, indicating that this appendage junction flow has a single horseshoe root vortex.

Little variation has been seen between flow parameters for either appendage shape. However, this conclusion does not hold when the shape of the leading edge is changed. Large variations are seen as a result of using a blunt leading edge. The driving forces for the secondary flow are due to the pressure gradients. In the last section it was seen that the elliptical nose increased the pressure gradients. As a result of these increases the horseshoe root vortex is stronger and creates greater cross-flow velocities. This is observed in the flow visualization on the flat plate. Comparing the oil film visualizations between the NACA appendage and the elliptical nose appendage (Figs. 9b and 14) one sees that the primary separation occurs at just about the same x position on the centerline. This result is expected since the pressure gradients along the centerline are similar for the two foil shapes. Differences are seen, however, in the favorable pressure region in the forward part of the appendages. The elliptical nose foil has a more curved separation line as a result of the more rounded geometry and greater cross-flow velocities. The oil dot visualizations give a clearer picture of the increased elliptical nose (over NACA) cross-flow velocities. Ahead of the leading edge the elliptical nose foil (Fig. 15) shows much stronger upstream flow of the oil dots than the NACA (Fig. 11b). In the pressure recovery region abaft maximum thickness, the elliptical nose foil also shows stronger outward flow. These differences are attributed to greater streamwise vorticity in the flow around the elliptical nose appendage.

VELOCITY MEASUREMENTS

The three-dimensional mean and fluctuating velocities were measured for the elliptical-leading-edge appendage. These measurements were taken at seven cross-flow planes in the inflow, appendage, and wake regions. In this section the velocity data will be discussed for each plane starting with the inflow and ending with the wake. The reference velocity (nominal free-stream velocity in the tunnel) for these measurements was 30.5 m/s resulting in a chord Reynolds number of approximately 500,000.

Inflow Plane $x/c = -0.75$

The nominal inflow condition for this geometry is a two-dimensional fully developed turbulent boundary layer. The upstream measurement plane was located at $x/c = -0.75$. The streamwise velocity contours are shown in Fig. 20 and show a reasonably uniform flow. The cross-flow velocity vectors (Fig. 21) show no cross flows greater than the confidence level for this flow. (It is important to note that the confidence limit is approximately plus or minus the size of the arrow heads, and that the magnitude of the velocity is represented by the length of the "shaft" of the arrow.) The turbulent kinetic energy contours shown in Fig. 22 are normal and reflect the small variations seen in the velocity contours. In this plane the 99% boundary-layer thickness is about 2.5 in. with a momentum thickness Reynolds number of approximately 15,000.

16

Appendage Plane X/C = 0.18

This measurement plane is located at the maximum thickness of the appendage. Fig. 20b (streamwise velocity contours) shows the essential features of the flow at this location. In the two-dimensional region of the foil (y > 3 in.), we see the accelerated flow close to the appendage which gradually drops off with increasing z as expected. In the two-dimensional region of the flat plate (z > 4 in.), we see a boundary layer similar to the inflow condition. In the junction region we see a uniform transition from the appendage flow to the wall flow with no large features due to the secondary flow. The only obvious effect of the horseshoe root vortex is a small "kink" in the contours close to the wall (y = 0.2 in.) near z = 2 in. The oil-film flow visualization at this location shows the primary separation line at z = 2.5 in. The conclusion from these last two observations is that the vortex has a flattened shape, small away from the wall but large across the wall. This same conclusion was reached by Pierce and McAllister,[12] for the flow ahead of the foil. The cross-flow velocity vectors (Fig. 21b) show the outflow, due to momentum effects, in the foil two-dimensional region. We can also see an outflow in the two-dimensional wall region due to pressure induced skewing of the boundary layer. In the corner we can see the cross-flow velocities created by the secondary flow vorticity. This flow is toward the wall along the appendage and out along the wall. Very high w velocities are seen close to the wall in the region where the oil dot visualization (Fig. 15) indicates high shear stress. The turbulent kinetic energy contours (Fig. 22b) show a slight inflow of outer less turbulent fluid into the corner region, and a "bubble" of more turbulent fluid being ejected in the separation region. In the velocity measurements at the x/c = 0.18 measurement plane, the small counter-rotating inner vortex seen in the flow visualization is not observed. This is due to the resolution of the hot-film probes and the dimensions of the measurement grid.

Appendage Plane x/c = 0.64

This measurement plane is located alongside the appendage in the pressure recovery region. The particular position was chosen to correspond with a measurement plane investigated using a LDV system.[17] The streamwise velocity contours are shown in Fig. 20c. In the two-dimensional region of the foil, we see a region of blocked flow but the intensity is greatly reduced from the previous measurement plane. The boundary layer has formed on the appendage but is still thin. The flow in the junction region looks significantly different from the contours at x/c = 0.18 in. The flow of high velocity fluid into the corner is seen. The outflow of low velocity fluid has distorted the contours near z = 2.25 in. It is evident that the secondary flow vorticity has effected a larger region. The primary separation line as seen in the oil films is located at z = 2.3 in., the location of the boundary-layer outflow. The cross-flow velocity vectors (Fig. 21c) show a flow toward the foil in the appendage two-dimensional region. This is expected due to the geometry of the foil abaft the location of maximum thickness. This inflow (in a cartesian coordinate system) is, to zero order, imposed across the wall boundary layer. The v velocity of the traverse closest to the appendage (z = 0.8 in.) may contain a negative bias due to

overcorrection for the effect of shear across the hot-film probe volume. In the two-dimensional region of the flat plate a small skewing of the boundary layer is seen due to the recovery region pressure gradients. In the secondary flow region a clockwise circulation is seen; however, due to the superimposed flow toward the appendage only one location (y = 0.1 in. and z = 2.0 in.) has a positive w velocity. (Also note that this velocity magnitude is less than the confidence level of the data.) Excellent agreement is found when comparing the position of minimum w velocity magnitude (z = 2.25 in.) with the location of the primary separation (z = 2.3). An interesting result is seen in the corner (y = 0.1, 0.2; z = 0.8 in.) where the v velocity is positive in spite of the apparent negative shear bias. These two measurements are probably in the inner counter-rotating vortex. The turbulent kinetic energy contours highlight the effect of the vorticity on the junction region. The low turbulent level outer fluid is injected near the appendage and the highly turbulent fluid is lifted away from the wall by the juncture flow.

This measurement plane was measured with a laser doppler anemometer system and reported previously by Dickinson.[17] Fig. 25 shows the u velocity profiles measured with the hot-films (see Volume II for similar plots of all the measurement planes) and Figs. 26a and 26b reproduce the LDV u velocity profiles for comparison. The velocities in the two-dimensional region outside the boundary-layers agree within one or two percent. In the flat plate boundary layer the velocity at y = 0.4 and z = 4.0 in. is the same for both measurement methods. In the secondary flow region y = 0.4 and z = 1.0 in., the LDV measured the streamwise velocity 5% higher than the hot film. In this region accelerations and deaccelerations are high and the clay particles for the LDV may not have followed the flow.

The w cross-flow velocities, Figs. 27 and 28, (the only cross-flow component measured with the LDV) match well between techniques; however, the LDV measurements are systematically 2% more negative than the hot-film measurements. Since this appears to be a systematic bias, it is probably due to either the LDV optical system alignment or the choice of the (arbitrarily defined zero cross flow) hot-film calibration location. Overall the author feels that the agreement between the LDV and the hot film is excellent considering the complication of the flow, the independence of the experiments, and the difference in transducers.

Appendage Plane x/c = 0.75

This measurement plane is located beside the appendage in the pressure recovery region. This particular region was chosen to be a reference location for numerical work and a common location for different experimentalists to compare data. As will be seen later in the streamwise direction, this location is in a region of slow change in the flow structure; therefore, the location represents a "pseudo-developed" flow.

The streamwise velocity contours are shown in Fig. 20d. In the two-dimensional region of the foil, the blocked flow has almost been diffused. The appendage boundary layer is thin but growing. The flow in the corner region is similar to the x/c = 0.64 plane with an inflow of high velocity fluid near the corner and an outflow of low velocity fluid near z = 2.0 in. The cross-flow velocity vectors,

Fig. 21d, are also similar to the previous measurement plane. The geometry induced inflow is seen in the two-dimensional region. The apparent overcorrection for shear is seen in the traverse closest to the foil. In the two-dimensional region of the flat plate the skewing of the w velocity is seen in the boundary layer. In the secondary flow area the inflow is seen in the corner and the outflow is seen near the separation line (z = 2.25 in. as determined by the oil film). The counter rotating vortex is not seen. The turbulent kinetic energy contours, Fig. 22d, are becoming more distorted but do not show any new features.

Appendage Plane x/c = 0.93

This measurement plane is located alongside the appendage in the pressure recovery region just ahead of the trailing edge. This location was chosen to be near the end of the smooth pressure recovery region, and represent the inflow to the high gradient trailing edge region.

The streamwise velocity contours are shown in Fig. 20e. These contours show the same features as the two previous measurement planes. The accelerated flow due to blockage has almost completely decayed, and the foil boundary layer has grown significantly. The inflow and outflow of fluid in the secondary flow region has lessened noticeably. This is probably due to the streamwise compression of the vortex tubes and the turbulent diffusion of momentum. Fig. 21e shows the cross-flow velocity vectors. The geometry induced inflow is seen in the two-dimensional region. The traverse closest to the appendage does not show the shear correction error seen in the two measurement planes upstream. This is a result of the thicker boundary layer and correspondingly reduced shear. In the two-dimensional region of the flat plate, the skewing of the boundary layer is noticeably reduced from the upstream locations. In the secondary flow region near the wall, four measurements around z = 1.75 show positive w velocities. This indicates that the horseshoe root vortex circulation is overcoming the geometry induced inflow. This is a result either of the integrated effect of the vorticity upstream or the pressure gradients near the trailing edge. The oil-film flow visualization showed the separation line at z = 2.15 in. This agrees well with the edge of the positive w velocity at 2.25 in. The counter-rotating vortex is not seen in the corner region. The turbulent kinetic energy contours, Fig. 22e, clearly show the effect of the vorticity on the boundary layer as it traversed the appendage. The low turbulent level outer fluid has been pumped in along the appendage to the corner, and the high turbulent level fluid has been ejected from the wall region in the vicinity of the primary three-dimensional separation.

Wake Plane x/c = 1.05

This measurement plane is located behind the appendage in the wake. This location was chosen to be in the near wake, and highlights the effects of the trailing edge. Large differences will be noted from the flow in the previous plane.

The streamwise velocity contours are shown in Fig. 20f. In the two-dimensional region of both the appendage and the flat plate, the flow is similar to the measurements alongside the appendage. Instead of a boundary layer, however, a

19

wake exists behind the foil. In the secondary flow region the inflow and outflow of fluid has continued to be reduced. A significant feature is seen in the corner region. The inflow is now convecting the low velocity appendage wake into the corner, resulting in an area of slow moving fluid near the wall at the centerline. This reduces the wall shear stress as can be seen in Fig. 11b. Fig. 21f shows the cross-flow velocity vectors. From $z = 3.0$ to $z = 5.0$ in. there is a systematic calibration error of the w velocity outside the stated accuracy. Justifiable corrections were made to these data, however, some error still remains. This error does not effect the other velocity components or the fluctuating w' measurements. The cross-flow vectors show a significantly modified picture of the flow when compared to the flow just upstream of the trailing edge. In the two-dimensional region of the appendage one now sees an outflow (positive w velocities) rather than the geometry induced inflow of the pressure recovery appendage measurement planes. The outflow is also seen in the oil dot flow visualization, Fig. 11b. The convection of the wake in the direction of the wall is seen and this effect in combination with the outflow almost reverses the direction of the secondary flow. The turbulent kinetic energy contours, at this measurement plane, are similar to the contours just upstream although the convection of fluid is reduced. This indicates that the mean secondary flow has a shorter time scale than the turbulence decay time scale. The oil-film flow visualization shows the primary separation line located at $z = 2.3$ in. in agreement with the location of high turbulent fluid ejection.

Wake Plane $x/c = 1.50$

This measurement plane is located behind the appendage in the wake. This location was chosen to be as far downstream as the experimental configuration allowed. The intention was to measure the far wake. Whether or not this was achieved is not known.

The streamwise velocity contours are shown in Fig. 20g. They illuminate the same features discussed previously. The vorticity induced inflow and outflow is decaying, lessening the distortion of the contours. In the appendage two-dimensional region, the wake is decaying, as seen by the reduced velocity deficit. The cross-flow velocity vectors, Fig. 21g, show that, at this location, there is no longer a geometrically induced cross flow. In the regions away from the wake and the wall there is no cross flow within the accuracy of the data (plus or minus the size of the arrow head). There appears to be a vortex-like circulation centered about $y = 1.0$, $z = 2.0$ in. It is important to note that there is no velocity magnitude associated with this feature, and, as will be shown later, this is not a horseshoe root vortex. The significant flow illustrated in Fig. 21g is the flow into the corner near the appendage wake and the flow away from the junction along the wall. These features are the junction induced secondary flow. Fig. 22g shows the turbulent kinetic energy contours in the wake. In contrast to the velocity contours, the turbulence contours show an increased effect due to the secondary flow. The turbulent kinetic energy field has a memory of what happened upstream. In this measurement plane the figure shows a region of closed contours where the inner boundary-layer fluid has

20

been ejected. The center of this highly turbulent parcel of fluid is over the position of the primary separation as determined by oil-film flow visualization.

VORTICITY CALCULATIONS

The formation of the horseshoe root vortex secondary flow is a result of pressure induced skewing of the incoming cross-flow vorticity. This incoming vorticity is created by the boundary-layer shear. As the vorticity interacts with the pressure gradients at the leading edge, the cross-flow (in the z direction) vorticity is rotated to have a component in the streamwise direction. The vortex filaments wrap themselves around the base of the appendage creating the forseshoe root vortex. If this vorticity organizes into a tube like structure, a vortex ("tornado") may result. It is important to note, however, that the vorticity does not have to form a vortex but can exist in a shear layer form.

The cross-flow velocity vector plots would show the presence of a vortex in a uniform flow. However, in the data reported here, there are geometrical effects in all of the measurement planes except at $x/c = 1.5$. The geometrical effects take the form of a generally uniform inflow or outflow (relative to the appendage and parallel to the z axis). This distorts the effect of a vortex type vector pattern. The calculation of vorticity involves the spatial derivatives and removes any uniform geometrical influence from the data.

The calculation of streamwise (x-axis) vorticity was made using the v and w data at the corners of a rectangular box. dv and dw were determined by the difference of the average values along the sides of the box, and dy and dz were determined by the size of the box. Then the streamwise vorticity was found $\omega_x = dw/dy - dv/dz$. The boxes used were determined by the position of the neighboring data locations. The vorticity value was assigned to the location of the center of the box. Dimensional data was used to calculate the vorticity and ω_x has dimensions of inverse seconds.

Taking derivatives of data has the effect of reducing systematic error; however, it causes point-to-point variations to be enhanced. In this experimental data set, measurements were taken along flat plate boundary-layer traverses. Velocity values in neighboring traverses are subject to calibration drift. Up to 0.5% data collection drift occurred between neighboring traverses. This drift causes error on the order of $50\ s^{-1}$ in the calculated vorticity value. In the streamwise vorticity plots, systematic errors in vorticity were removed by requiring the vorticity in the two-dimensional region to be "low," a condition of reasonableness. The remaining estimated error band for the vorticity contour, Figs. 29-34, is one contour interval.

Fig. 29 shows the streamwise vorticity contours for measurement plane $x/c = 0.18$. There are two primary features shown at this location. First, one notes the primary horseshoe root vortex which has extremely strong negative vorticity. This feature is flattened along the wall as was previously deduced from the streamwise velocity contours. This flattened shape was also deduced from LDV measurements along the plane of symmetry[17] and called a "tank track" vortex. The second feature is the region of positive vorticity near the wall away from the appendage. This feature is believed to be caused by the outer fluid circulating into the primary

21

separation. Downstream at $x/c = 0.64$, Fig. 30, the streamwise vorticity field has changed. The primary vorticity region has become more rounded and lifted up off the wall. In the corner, a small region of positive vorticity has appeared indicating the presence of the counter-rotating vortex. The positive wall vorticity now occupies the region outside the primary separation. Further downstream at $x/c = 0.75$, Fig. 31, the vorticity field is essentially the same. Just upstream of the trailing edge at $x/c = 0.93$, Fig. 32, the streamwise vorticity pattern has developed further. The strongest negative vorticity, associated with the primary vortex structure, is next to the wall. Also the positive vorticity region of the counter-rotating vortex has lifted off the wall by a small distance. This explains why this feature disappears from the wall flow visualizations alongside the aft portion of the appendage.

In the near wake measurement plane, $x/c = 1.05$, Fig. 31, the streamwise vorticity field is complicated by the outflow (away from the $z = 0$ plane of symmetry). This outflow turns some of the cross-flow boundary layer vorticity into positive streamwise vorticity. In the previously discussed planes, the same effect was present (the effect was negative), but the vorticity measured for the planes could be compared to each other because the effects were similar. The outflow-caused positive vorticity dominates much of the junction region in the near wake measurement plane. However, near the wall the negative streamwise vorticity created by the secondary flow is still seen. The systematic error in the w velocities for some of this measurement plane mentioned earlier does not effect this vorticity calculation, due to the direction of the spatial derivative. This measurement plane indicates the need for care in interpreting vorticity results when only one component is analyzed and the coordinate system is not a local streamline coordinate system.

The downstream wake measurement plane $x/c = 1.5$, does not have the effect of inflow or outflow. The streamwise vorticity field is shown in Fig. 34. The field consists of a negative zone in the region inside both the primary separation and the boundary layer. There is also a small positive zone at the wall along the centerline. This positive region is the counter-rotating vorticity which had been lifted off the wall and has now been convected, by the downwash, back to the wall. The intense negative vorticity is close to the wall, relatively flat, and inside the "vee" shaped pattern as seen in the oil-film flow visualization. At this plane the magnitude of the streamwise vorticity has been reduced somewhat but the area of the effect has been enlarged.

As mentioned at the beginning of this section, vorticity can exist independent of a vortex. Indeed, this appears to be the case for the model examined in this research. The secondary flow structure in this work has been named a horseshoe root vortex, however, this name is misleading. Examination of the two components of the streamwise vorticity (dw/dy and $-dv/dz$) shows that the main vorticity feature (the intense negative vorticity region) never has the balance between the components that one would expect for a "tornado" type vortex. Virtually all of the vorticity is a result of the dw/dy component indicating a cross flow shear layer parallel to the wall. The only region where the vorticity components achieve a balance is in the corner where both wall and appendage cross flow shear layers exist. Also, at this

random directions. These observations indicate a vortex at the leading edge that breaks down. The measurements reported here indicate that the vorticity in the vortex becomes a shear layer flow after the breakdown.

SUMMARY

This report has presented results from an extensive experimental study of appendage-flat plate junctions. During this study two appendage shapes were investigated in turbulent flow, at zero degree angle of attack, with two boundary-layer thicknesses and three free stream velocities. Flow visualization was performed for all cases, and flat plate static pressure was measured for most of the cases. Three dimensional velocity measurements were made on seven planes at one speed for the elliptical nose appendage. These detailed measurements document the flow in an attempt to understand its physics, and to serve as a test case for numerical modeling.

Several observations were made about this flow.
1. For a given appendage, changing the free-stream velocity or the boundary-layer thickness did not change the flow at the wall.
2. Changing the curvature of the leading edge significantly changes the cross-flow velocities in the separated region. The blunter the appendage nose, the stronger the cross flow.
3. The pressure gradients are the primary driving forces in the junction flow.
4. The features of the secondary flow inside the three-dimensional separation consist of a primary vortex or *vorticity region* and a small counter-rotating vortex or vorticity region in the corner.
5. The primary vorticity in the secondary flow is close to the wall and flattened.
6. The turbulence decay time scale of the separated flow is greater than the secondary flow development time scale in the trailing edge region of the appendage.
7. The term vortex is an incorrect description for much of this flow. The horseshoe root vortex secondary flow appears to become shear layers abaft the position of maximum thickness of the appendage.
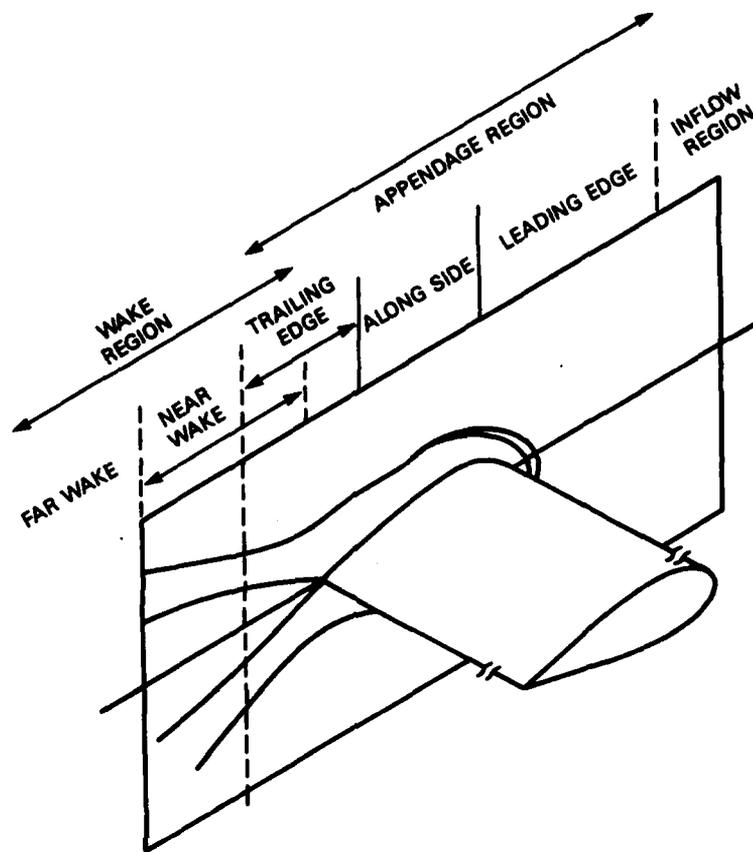
Fig. 1. Sketch of the appendage-flat plate junction flow regions.

Fig. 2. Model in the LTWT.

1.5 : 1 ELLIPTICAL NOSE

NACA 0020
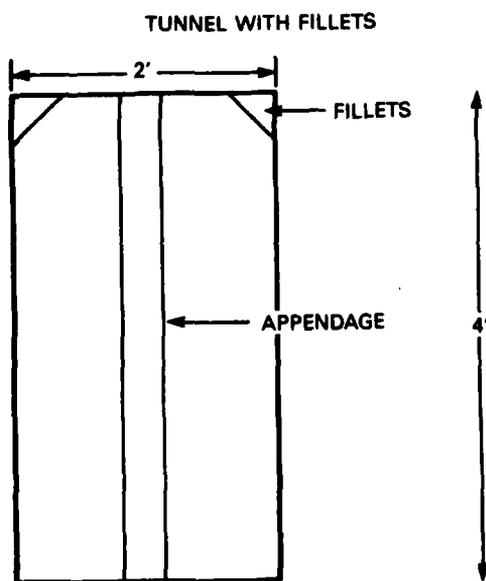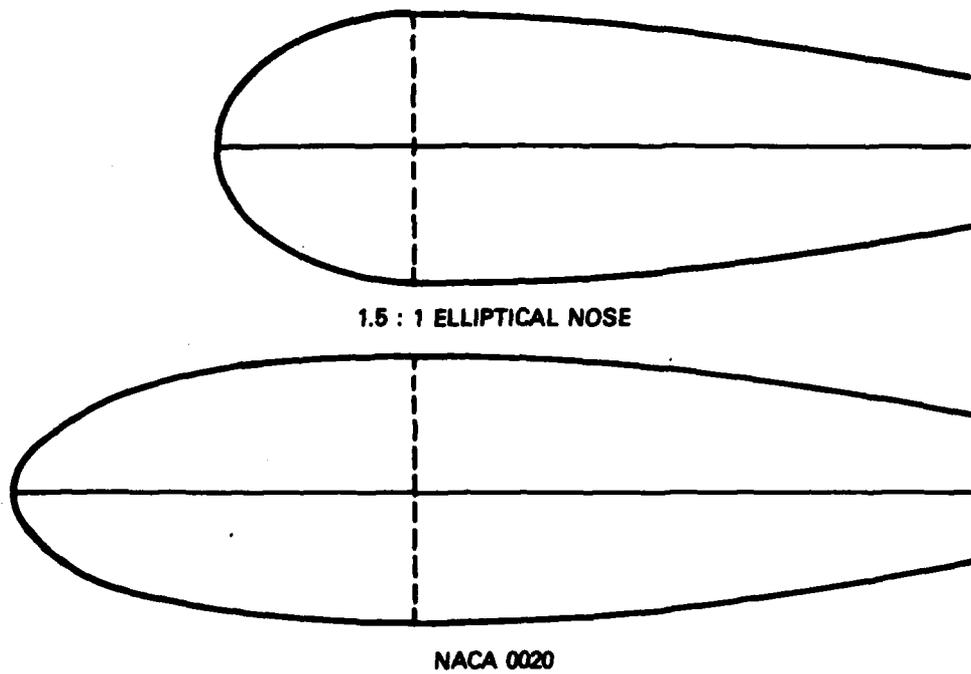
Fig. 3. Leading edges of the two appendages investigated.
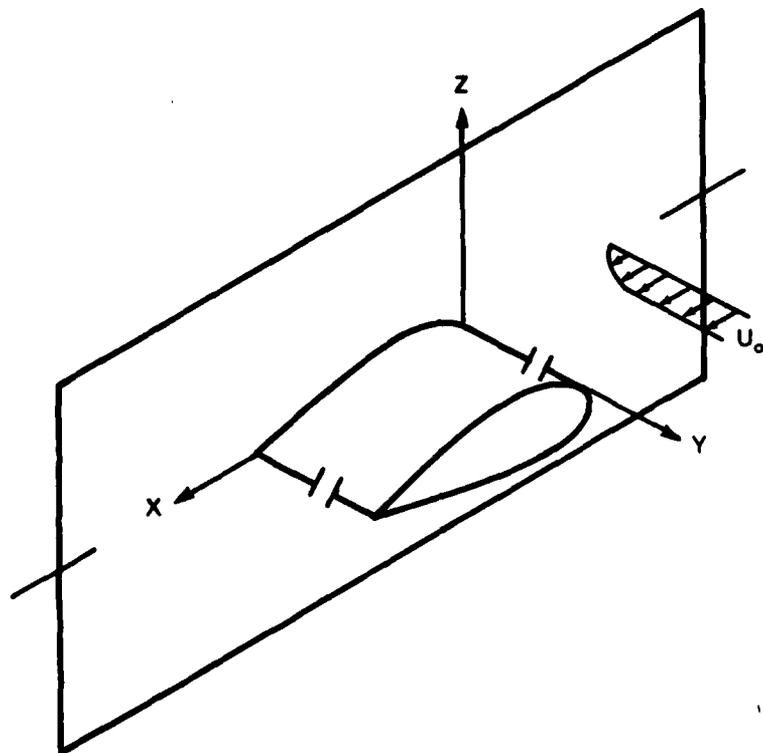
Fig. 4. Coordinate system.
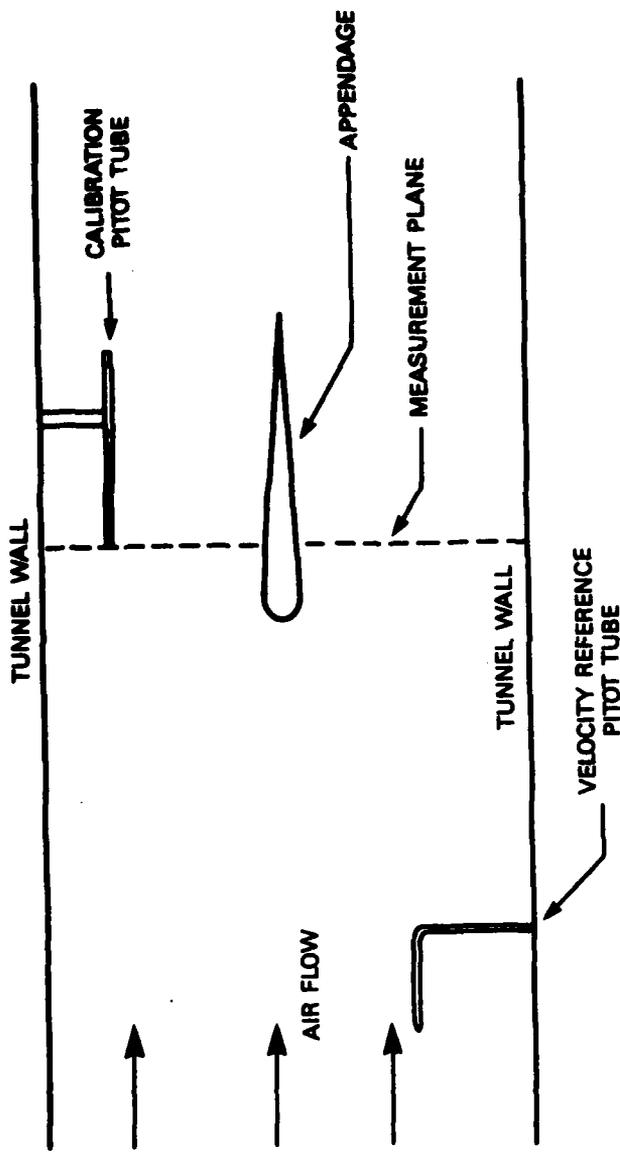
Fig. 5. Pitot tube locations.
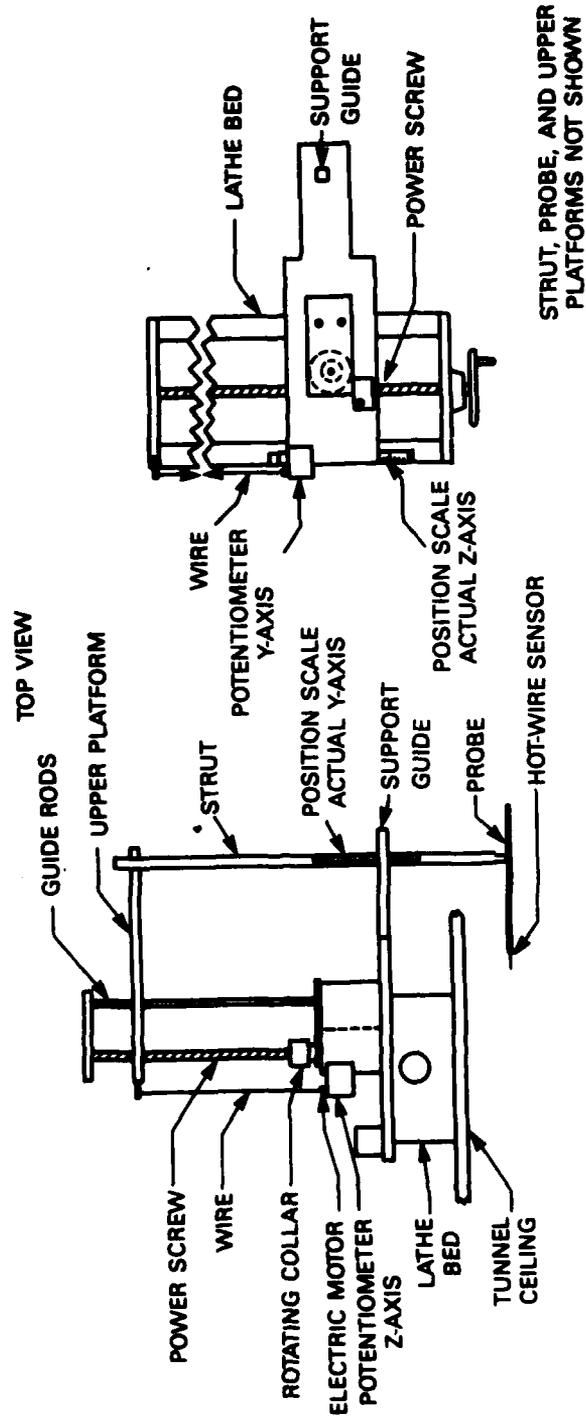
Fig. 6. Traverse Apparatus.

26
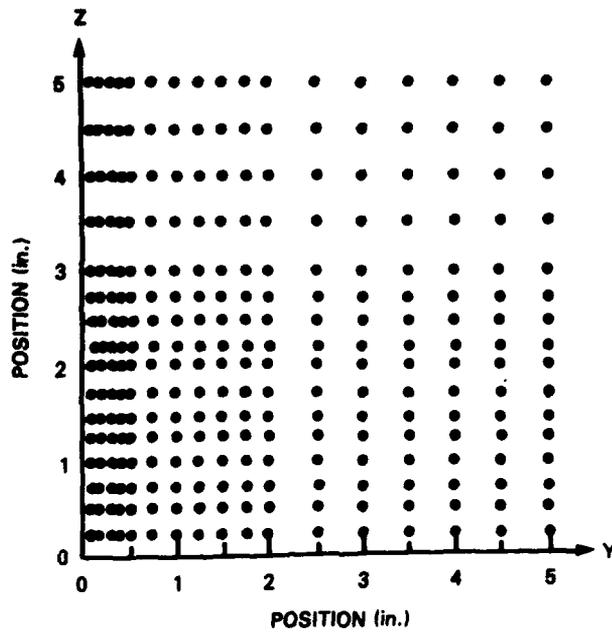
Fig. 7. Typical data collection grid.
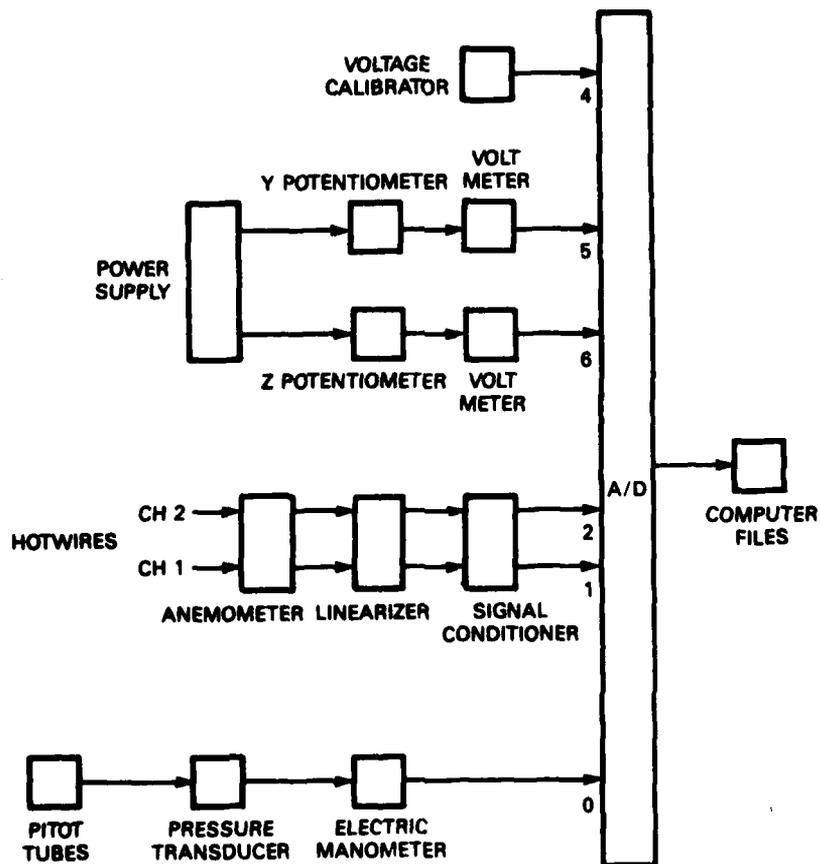
Fig. 8. Block diagram of data collection system.

1000 rpm
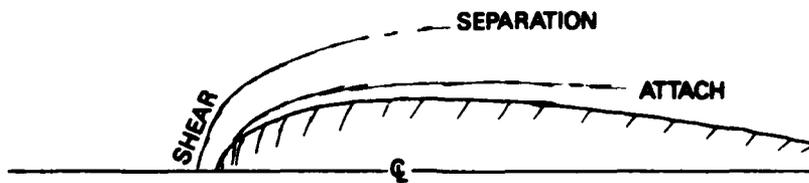
Fig. 9a. u_{ref} = 23.5 m/s, thick b-l.

1300 rpm
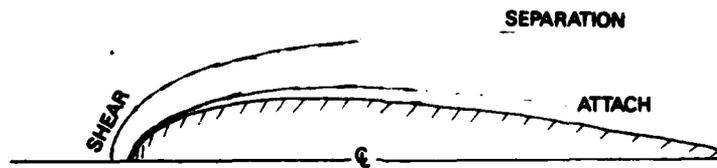
Fig. 9b. u_{ref} = 30.5 m/s, thick b-l.

1600 rpm
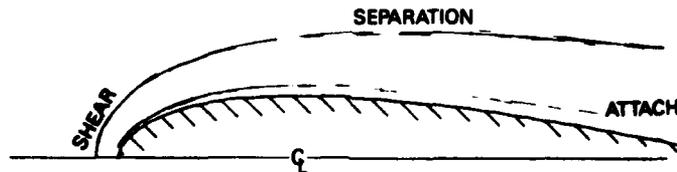
Fig. 9c. u_{ref} = 35.2 m/s, thick b-l.

Fig. 9. Sketch of oil film separation and attachment lines—NACA 0020.

1300 rpm
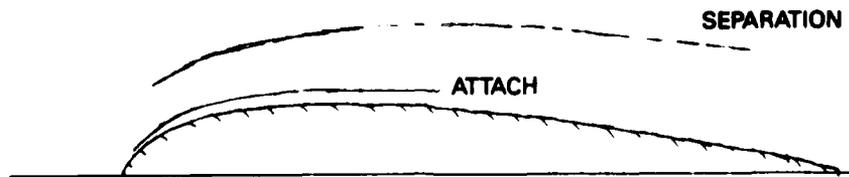
Fig. 10. Sketch of oil film separation and attachment lines as determined from oil dots—NACA 0020. u_{ref} = 30.5 m/s, thick b-l.

28

Fig. 11b. u_{ref} = 30.5 m/s, thick b-l.

Fig. 11d. u_{ref} = 30.5 m/s, thin b-l.
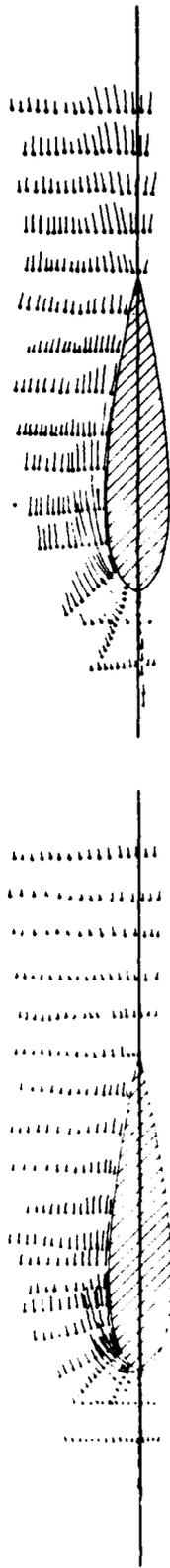
Fig. 11a. u_{ref} = 23.5 m/s, thick b-l.
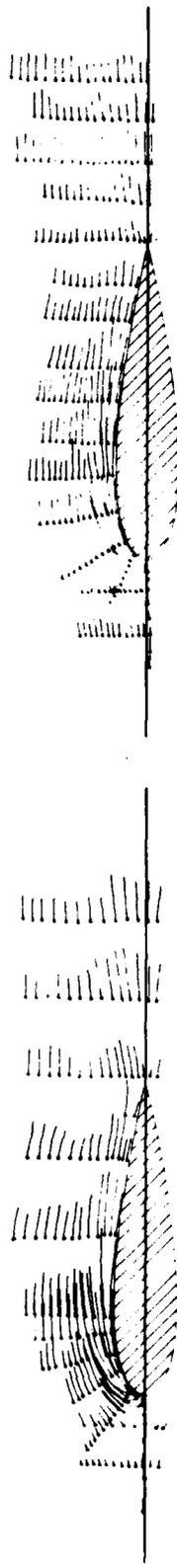
Fig. 11c. u_{ref} = 35.2 m/s, thick b-l.

Fig. 11. Oil-dot flow visualization—NACA 0020.
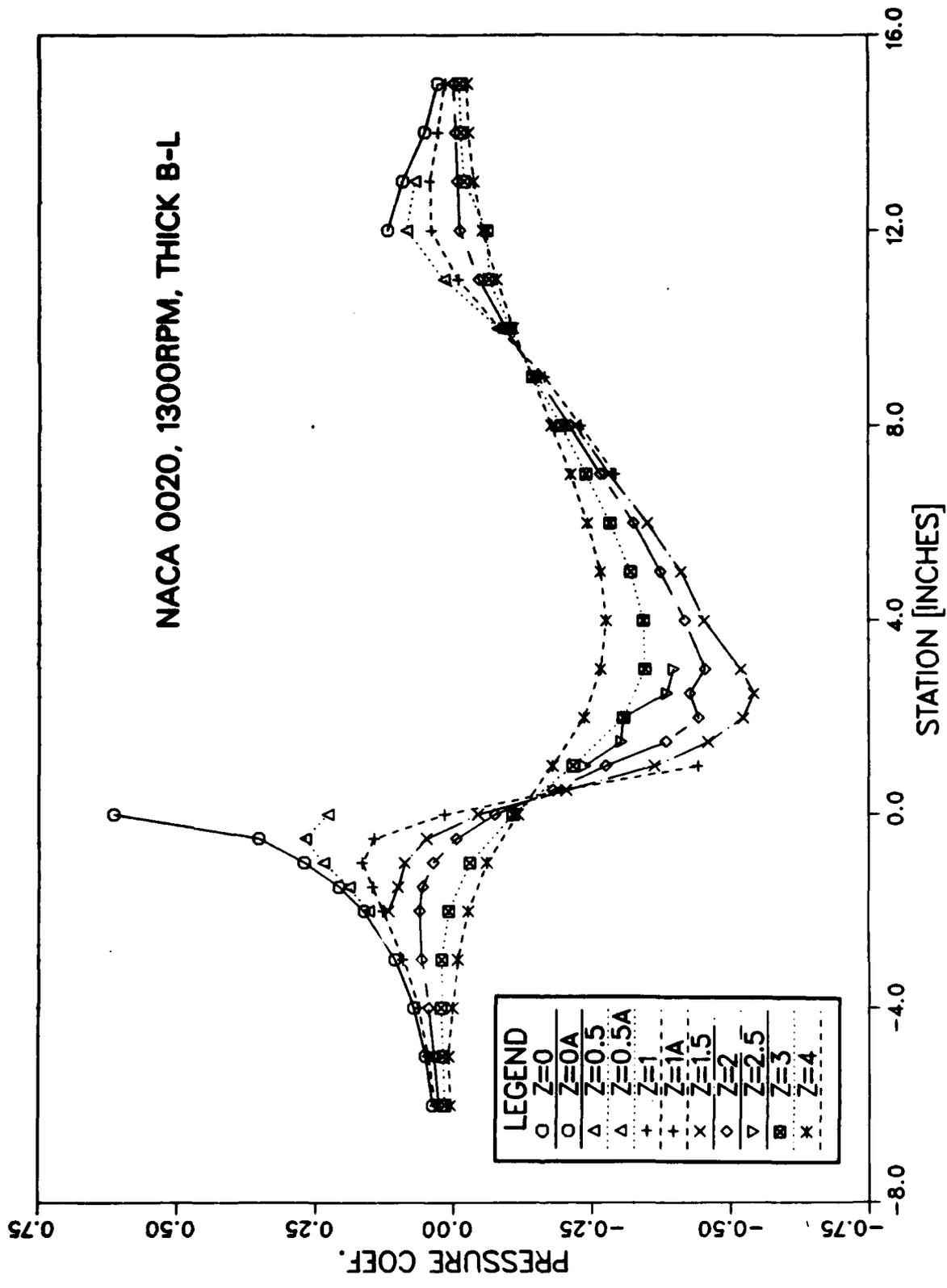
Fig. 12. Static pressure coefficients on the flat plate—NACA 0020. $u_{ref} = 30.5$ m/s, thick b-l
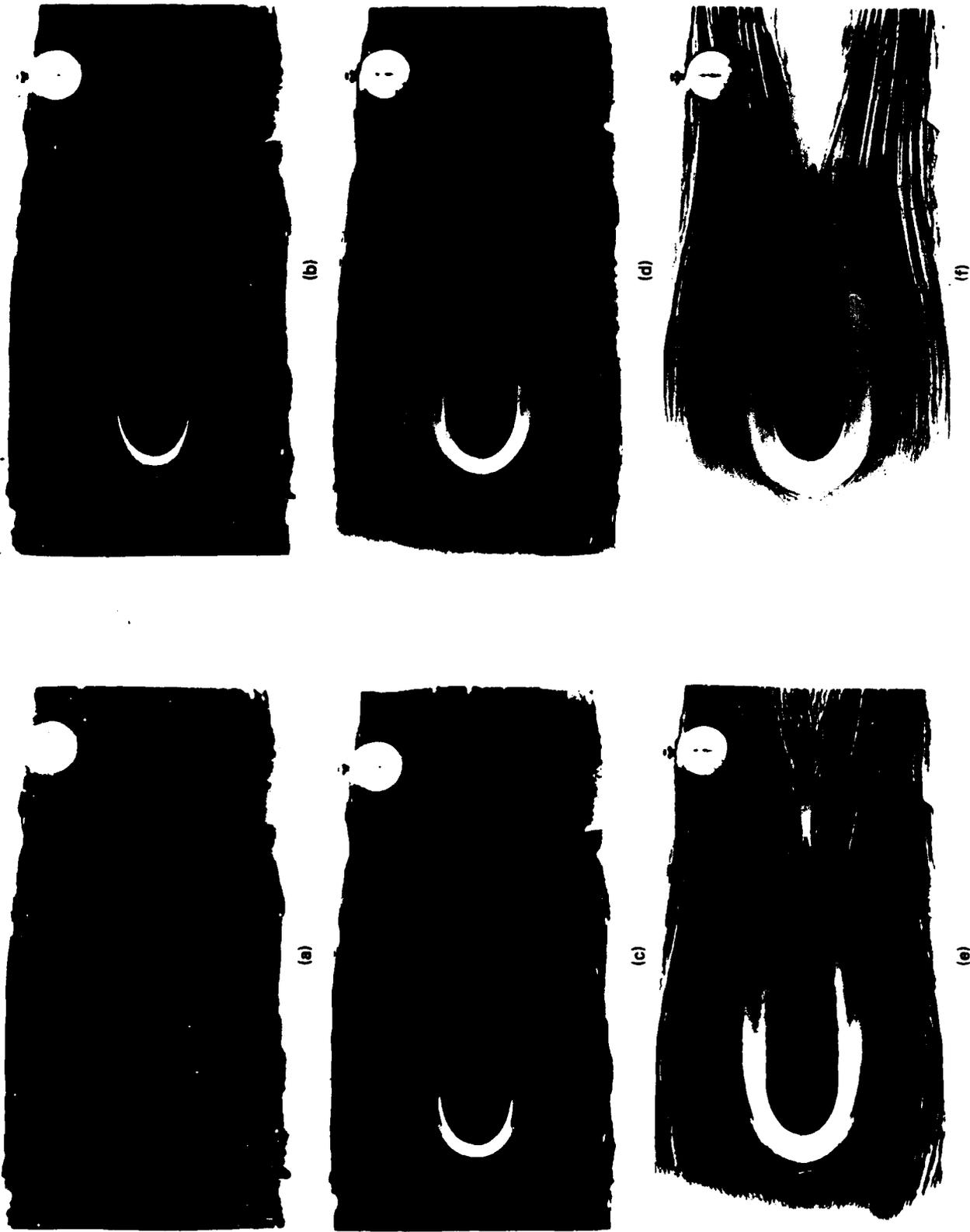
Fig. 13. Oil-film flow visualization of the elliptical nose appendage on the flat plate at time T after the flow is started. (a) T = 0 s, (b) T = 30 s, (c) T = 1 min, (d) T = 4 min, (e) T = 10 min, (f) T = 40 min.

31
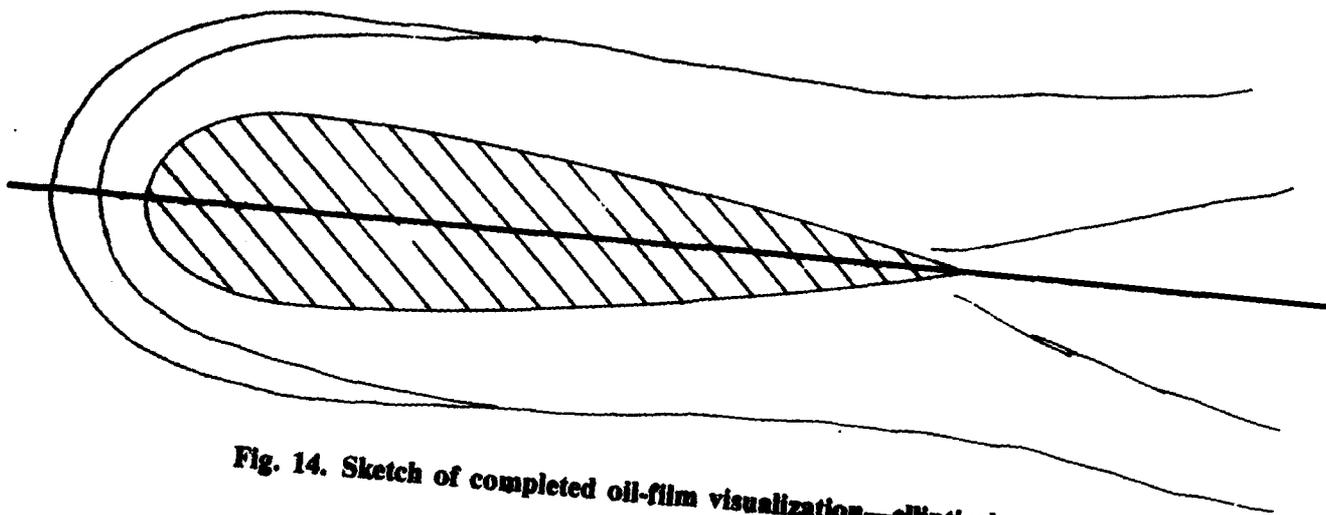
Fig. 14. Sketch of completed oil-film visualization—elliptical nose.
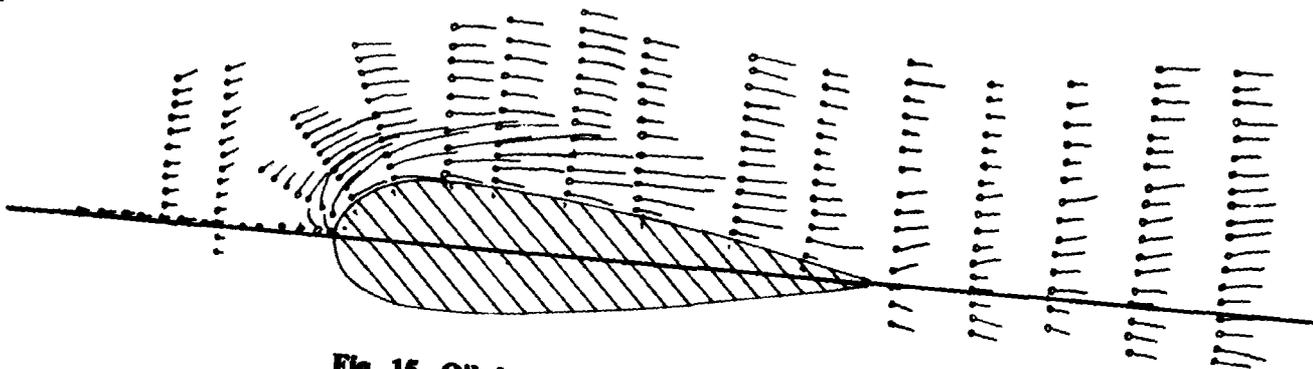
Fig. 15. Oil dot visualization pattern—elliptical nose.
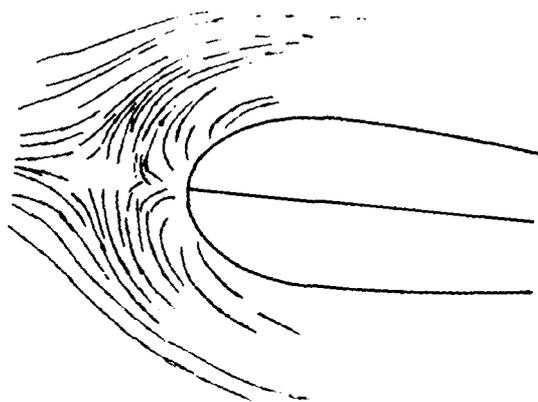
Fig. 16. Sketch of oil of wintergreen visualization—elliptical nose.
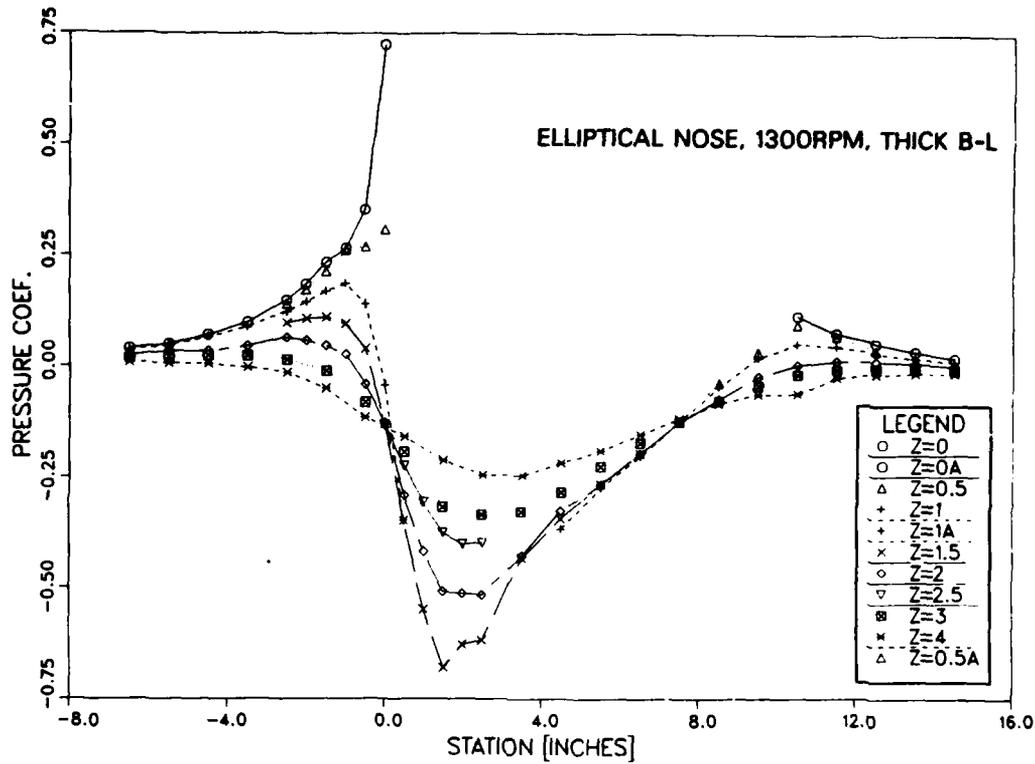
Fig. 17. Static pressure coefficients on the flat plate—elliptical nose.
u_{ref} = 30.5 m/s, thick b-l.
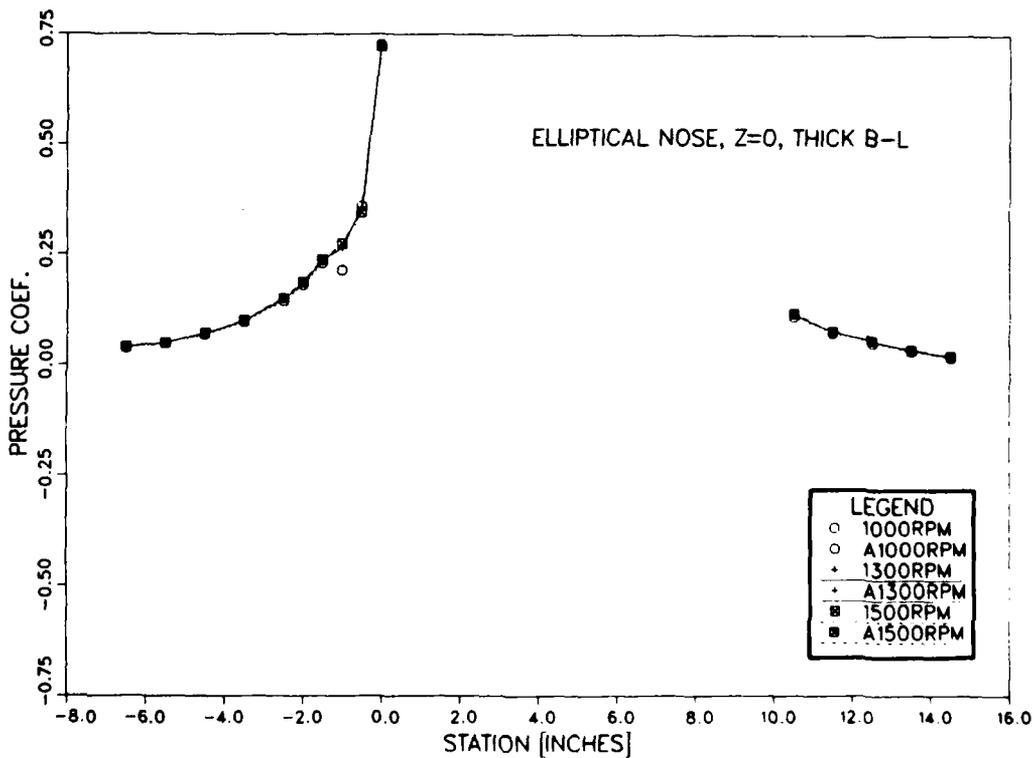
Fig. 18a. z = 0 in.

Fig. 18. Static pressure coefficients on the flat plate—elliptical nose.
Comparison between u_{ref} = 23.5, 30.5, 35.2 m/s.

33
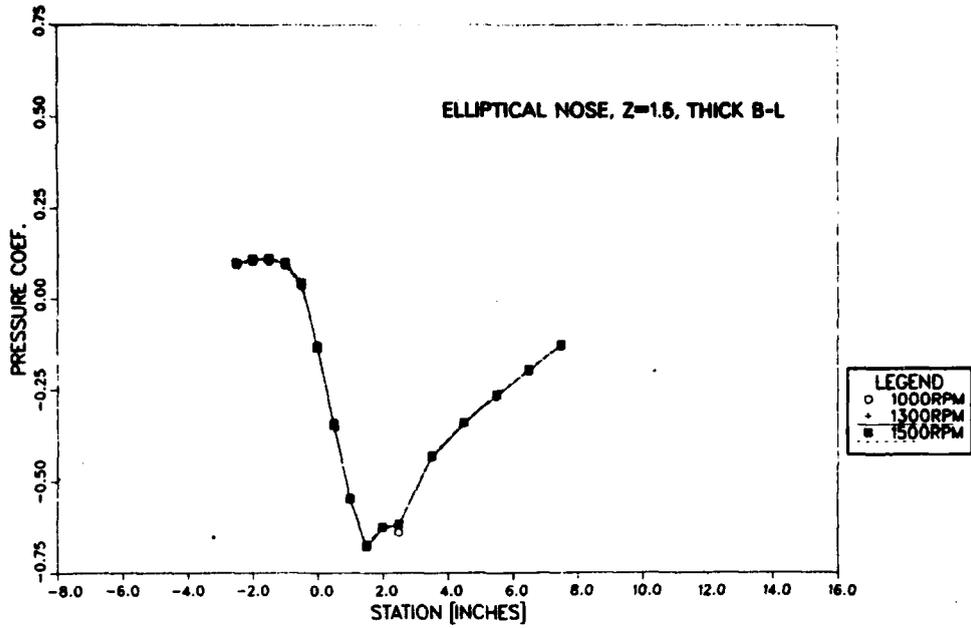
Fig. 18b. z = 1.5 in.
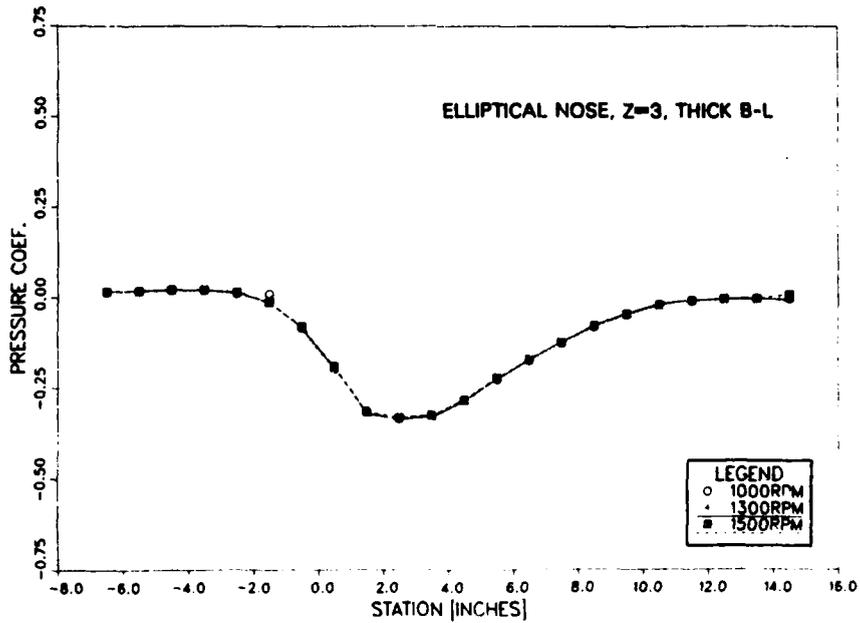
Fig. 18c. z = 3.0 in.

Fig. 18. (Continued)

34
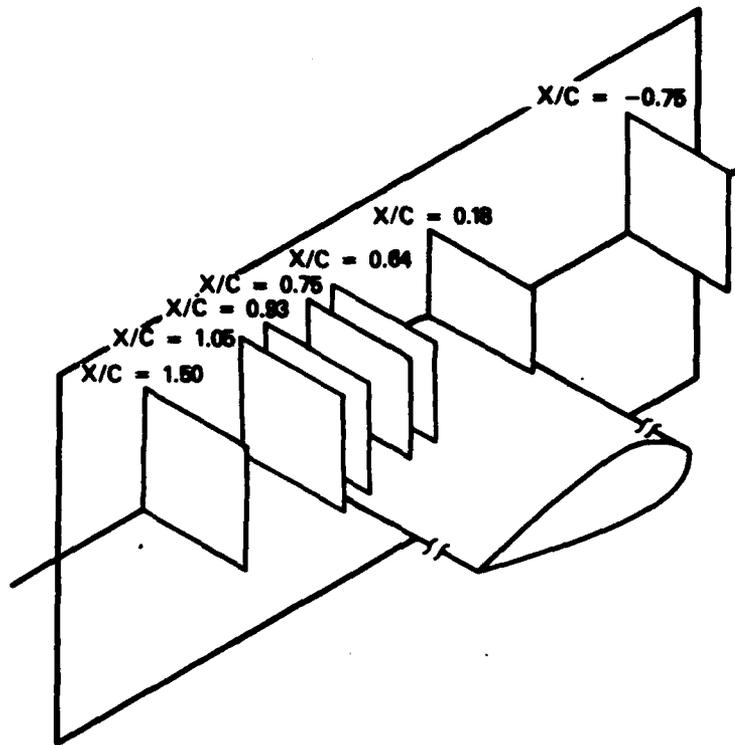
Fig. 19. Sketch of measurement planes where velocity measurements were made—elliptical nose.

STREAMWISE VELOCITY CONTOURS
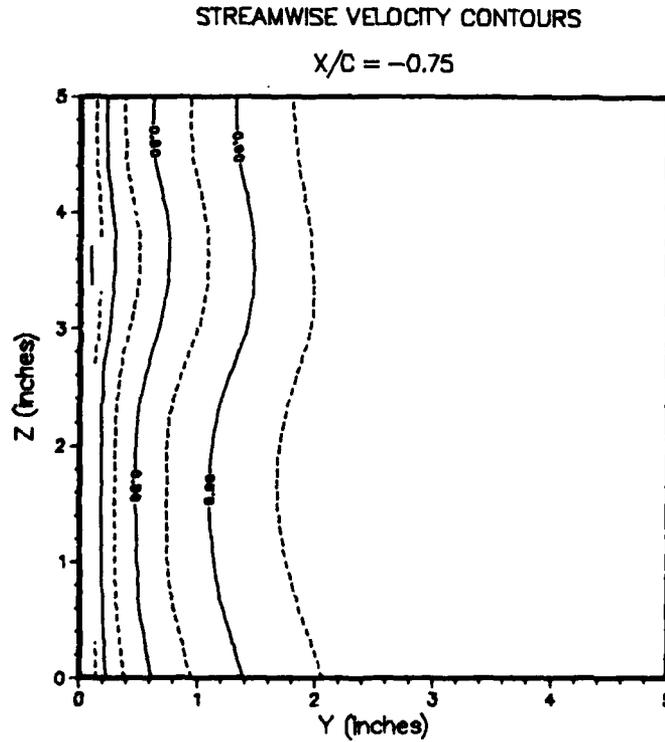
$X/C = -0.75$

Fig. 20a. x/c = -0.75.

Fig. 20. Streamwise velocity contours—elliptical nose.

35
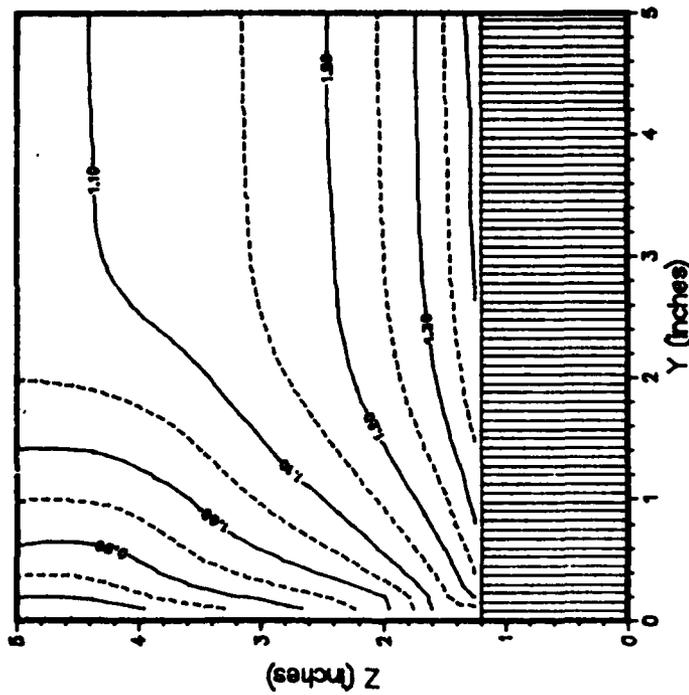
STREAMWISE VELOCITY CONTOURS

X/C = 0.64

Fig. 20c. x/c = 0.64

STREAMWISE VELOCITY CONTOURS

X/C = 0.18

Fig. 20b. x/c = 0.18.

Fig. 20. (Continued)

36
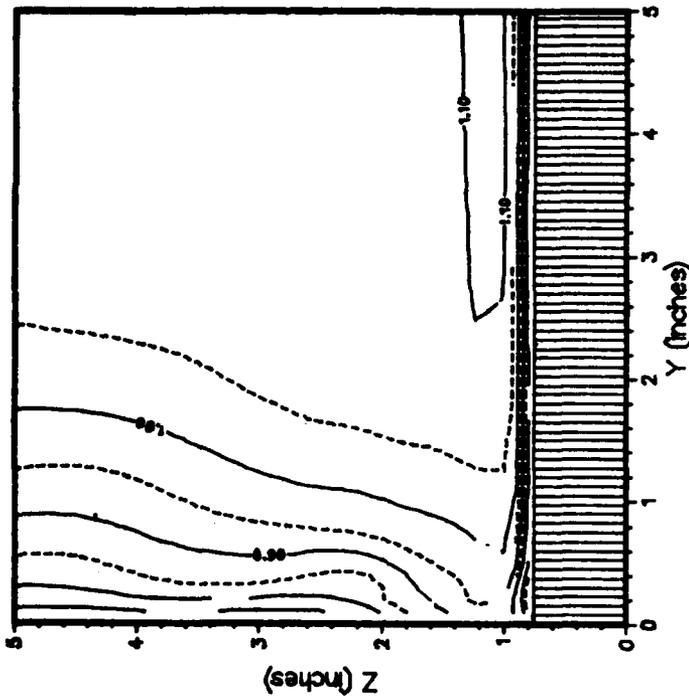
STREAMWISE VELOCITY CONTOURS
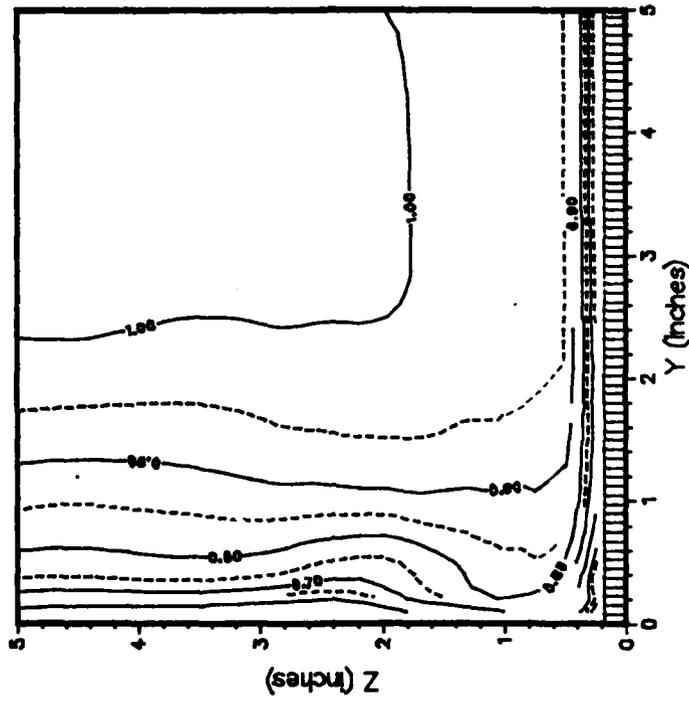
X/c = 0.93

Fig. 20e. x/c = 0.93.

STREAMWISE VELOCITY CONTOURS
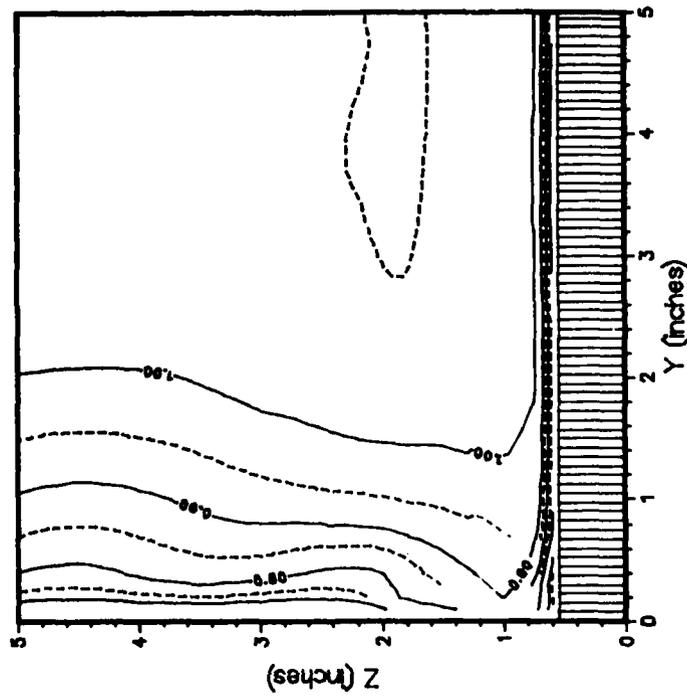
X/c = 0.75

Fig. 20d. x/c = 0.75.

Fig. 20. (Continued)

37

STREAMWISE VELOCITY CONTOURS

X/C = 1.50

Z (Inches)

Y (Inches)

Fig. 29g. x/c = 1.50.

STREAMWISE VELOCITY CONTOURS

X/C = 1.05

Z (Inches)

Y (Inches)

Fig. 29f. x/c = 1.05.

Fig. 29. (Continued)

38

CROSS-FLOW VELOCITY VECTORS

X/C = 0.18

Z (inches)

Y (inches)

Fig. 21b. x/c = 0.18.

0.1

CROSS-FLOW VELOCITY VECTORS

X/C = -0.75

Z (inches)

Y (inches)

Fig. 21a. x/c = -0.75.

0.1
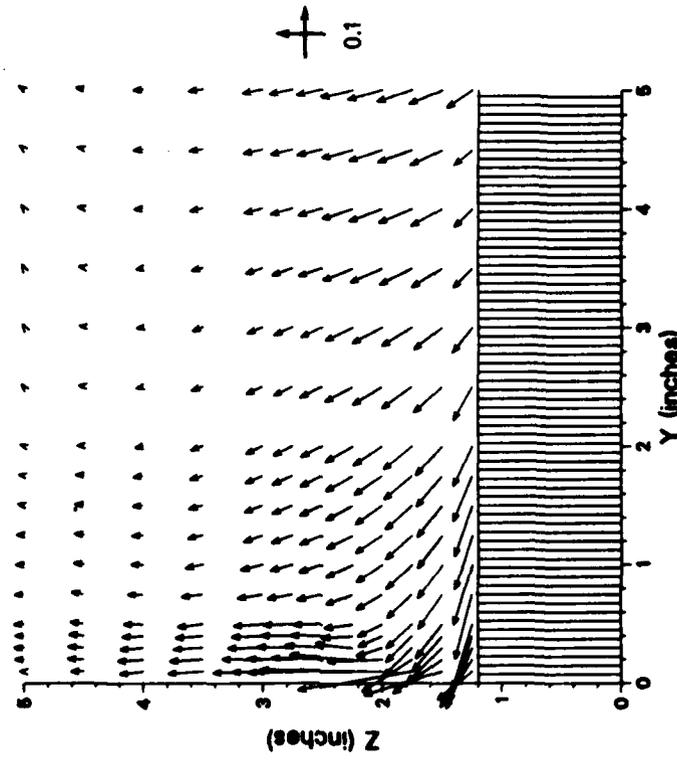
Fig. 21. Cross-flow velocity vectors—elliptical nose.

39

CROSS-FLOW VELOCITY VECTORS

X/C = 0.75

Z (inches)

Y (inches)

0.1

Fig. 21d. x/c = 0.75.

CROSS-FLOW VELOCITY VECTORS

X/C = 0.64

Z (inches)

Y (inches)

0.1

Fig. 21c. x/c = 0.64.

Fig. 21. (Continued)

CROSS-FLOW VELOCITY VECTORS

X/C = 1.05

Z (inches)

Y (inches)

Fig. 21f. x/c = 1.05.

CROSS-FLOW VELOCITY VECTORS

X/C = 0.93

Z (inches)

Y (inches)

Fig. 21e. x/c = 0.93.

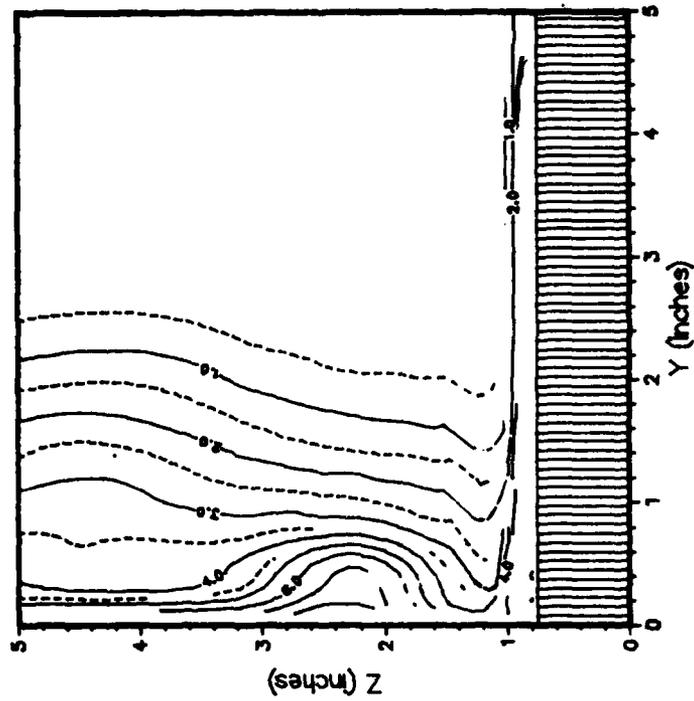Fig. 21. (Continued)

41

TURBULENT KINETIC ENERGY CONTOURS
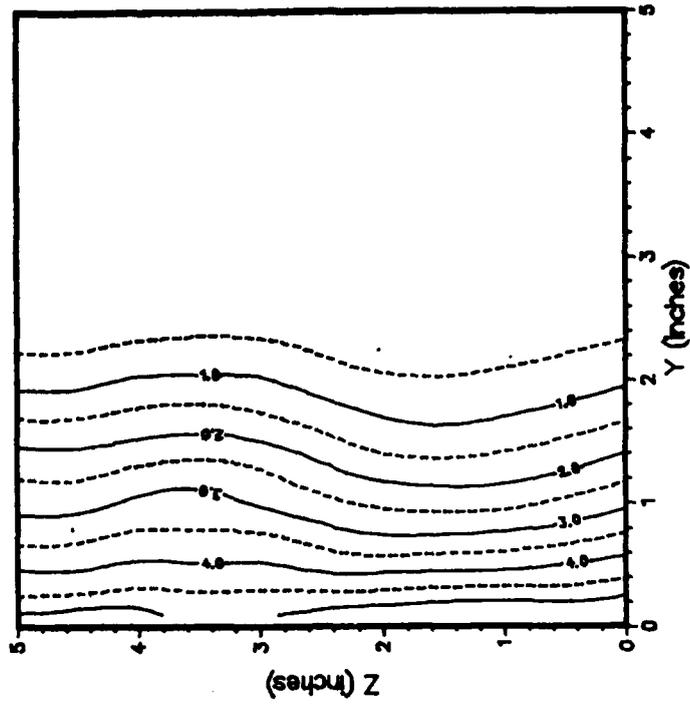
(TIMES 1000)
X/C = −0.75

Fig. 22a. x/c = −0.75.

Fig. 22. Turbulent kinetic energy contours—elliptical nose.

CROSS-FLOW VELOCITY VECTORS

X/C = 1.50
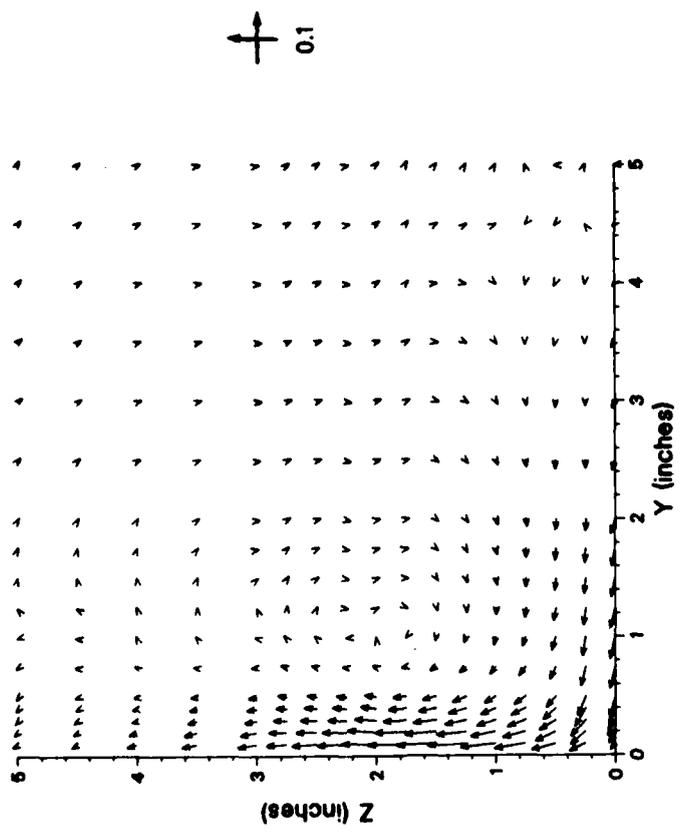
Fig. 21g. x/c = 1.50.

Fig. 21. (Continued)

42

TURBULENT KINETIC ENERGY CONTOURS
(TIMES 1000)
X/C = 0.64
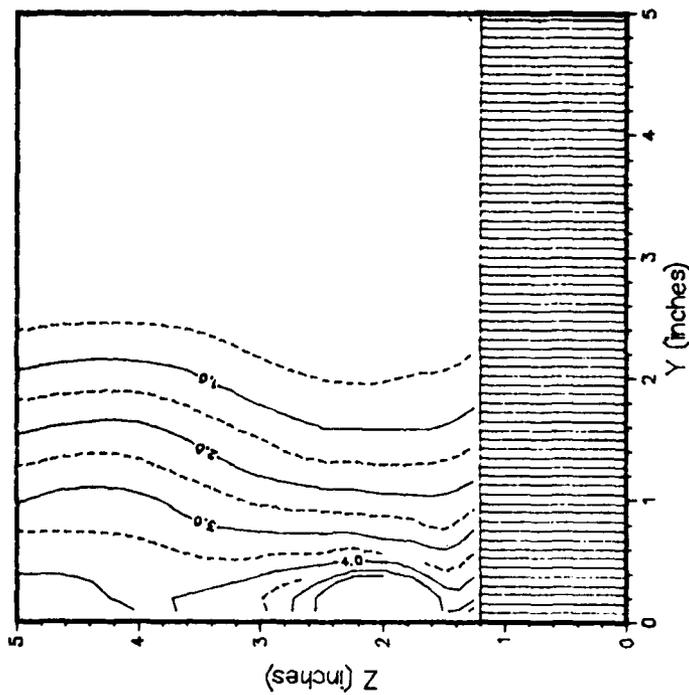
TURBULENT KINETIC ENERGY CONTOURS
(TIMES 1000)
X/C = 0.18

Fig. 22c. x/c = 0.64.

Fig. 22b. x/c = 0.18.

Fig. 22. (Continued)

43

TURBULENT KINETIC ENERGY CONTOURS
(TIMES 1000)
X/C = 0.93
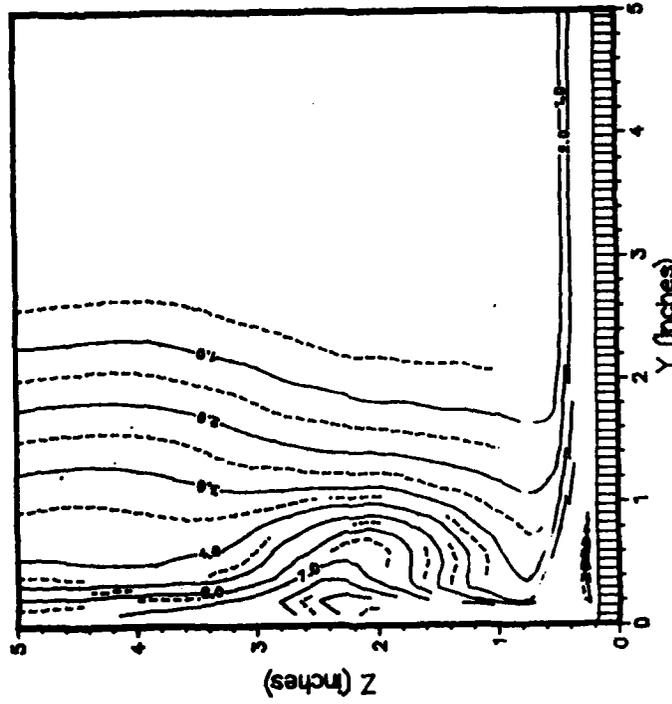
Fig. 22e. x/c = 0.93.
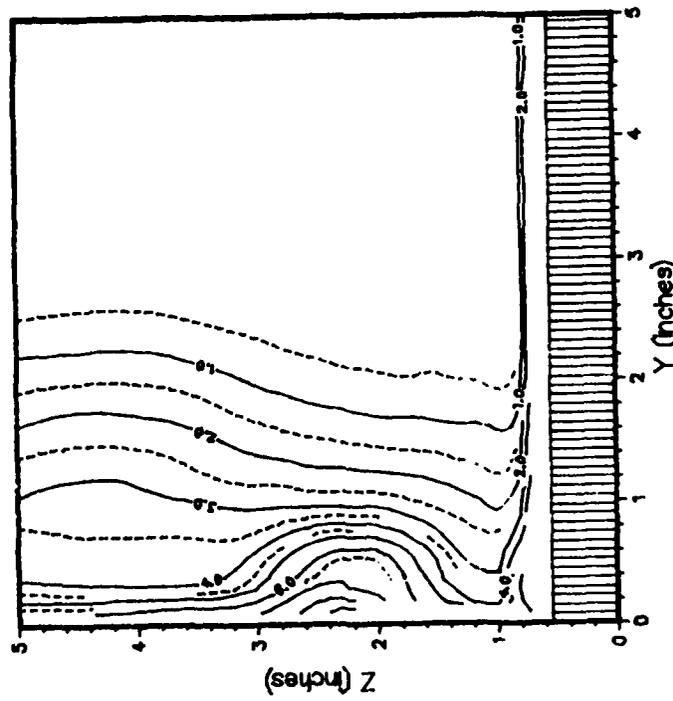
TURBULENT KINETIC ENERGY CONTOURS
(TIMES 1000)
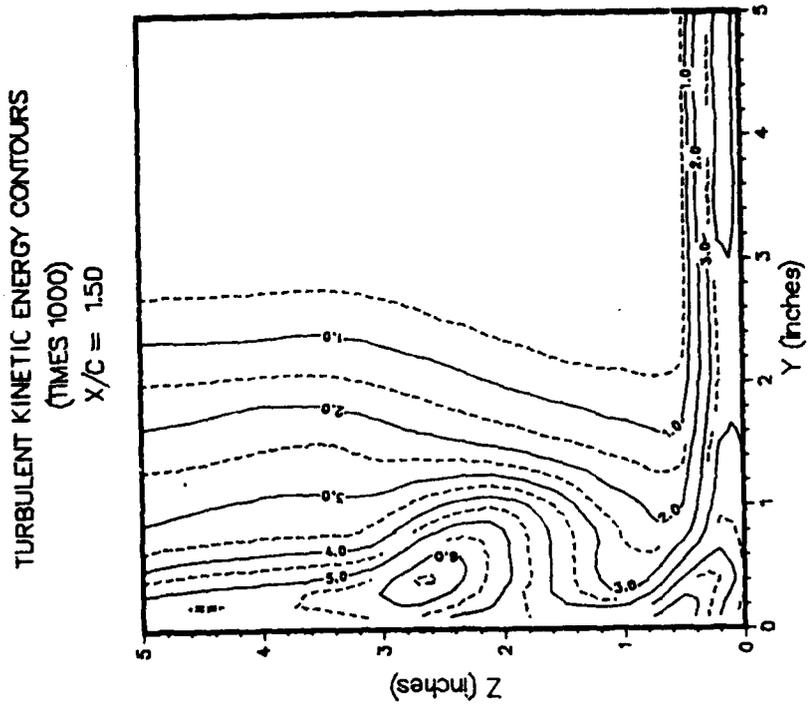X/C = 0.75

Fig. 22d. x/c = 0.75.

Fig. 22. (Continued)

44

TURBULENT KINETIC ENERGY CONTOURS
(TIMES 1000)
X/C = 1.50

Fig. 22g. x/c = 1.50.

TURBULENT KINETIC ENERGY CONTOURS
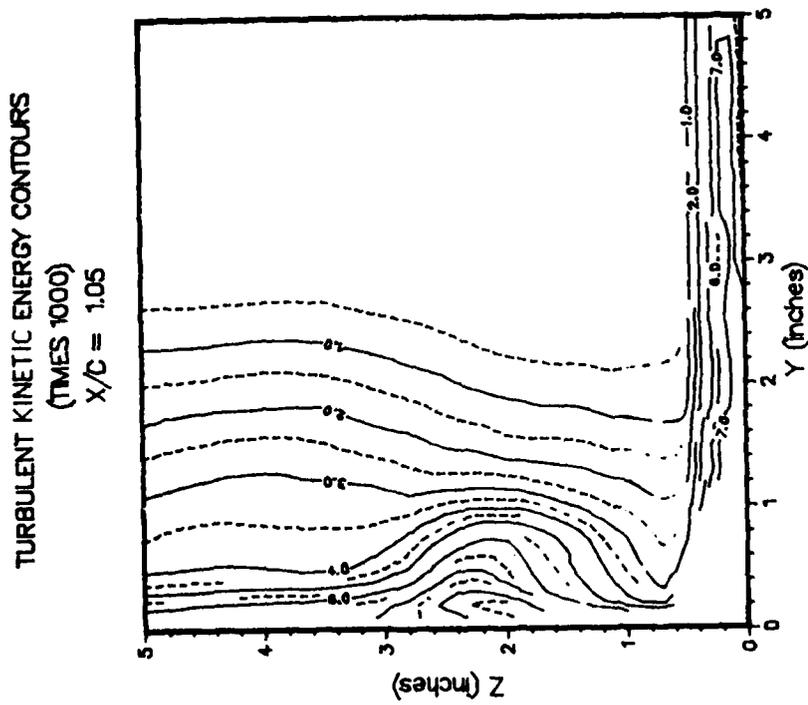(TIMES 1000)
X/C = 1.05

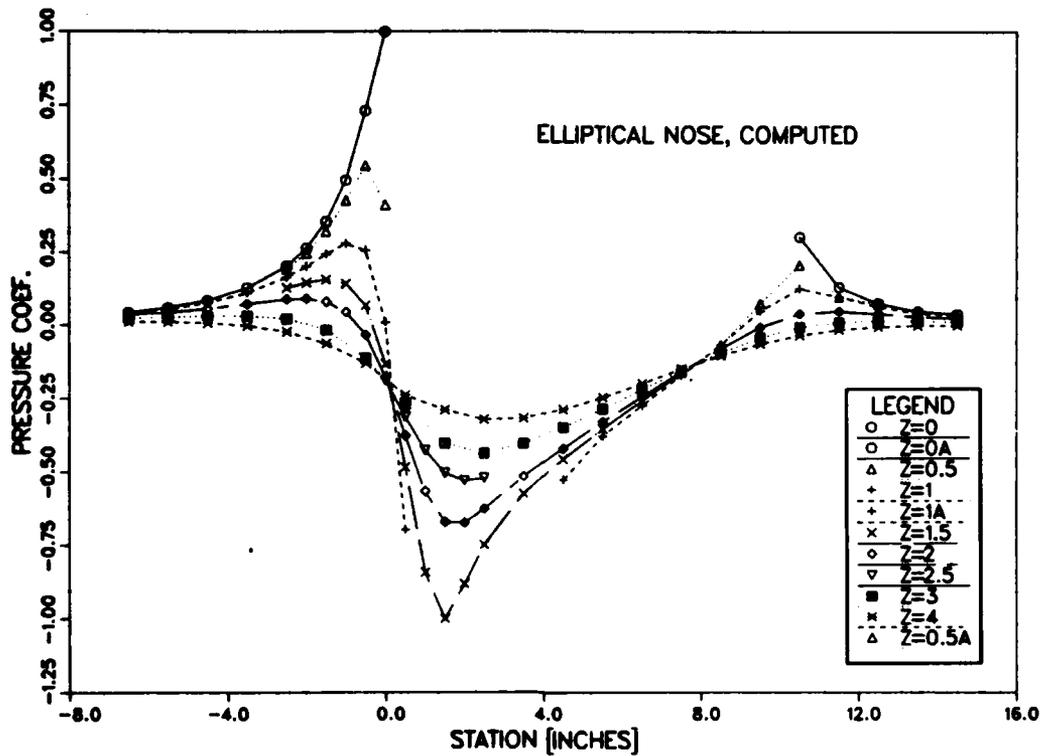Fig. 22f. x/c = 1.05.

Fig. 22. (Continued)

45

Fig. 23. Computed static pressure coefficients on the flat plate—NACA 0020.
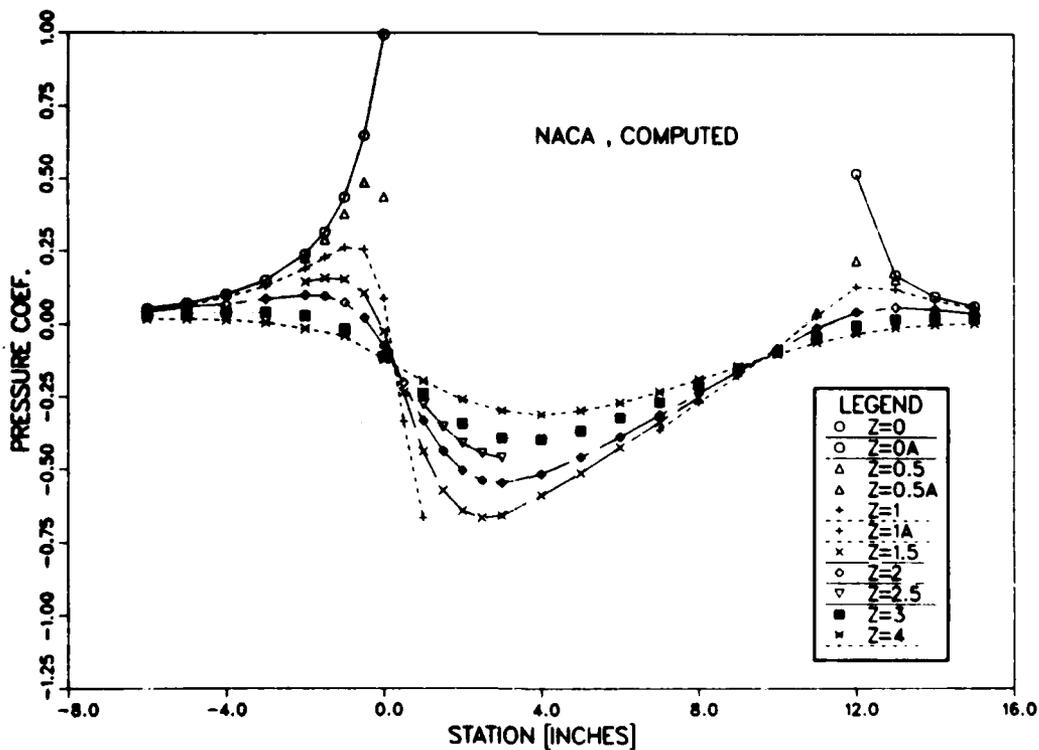

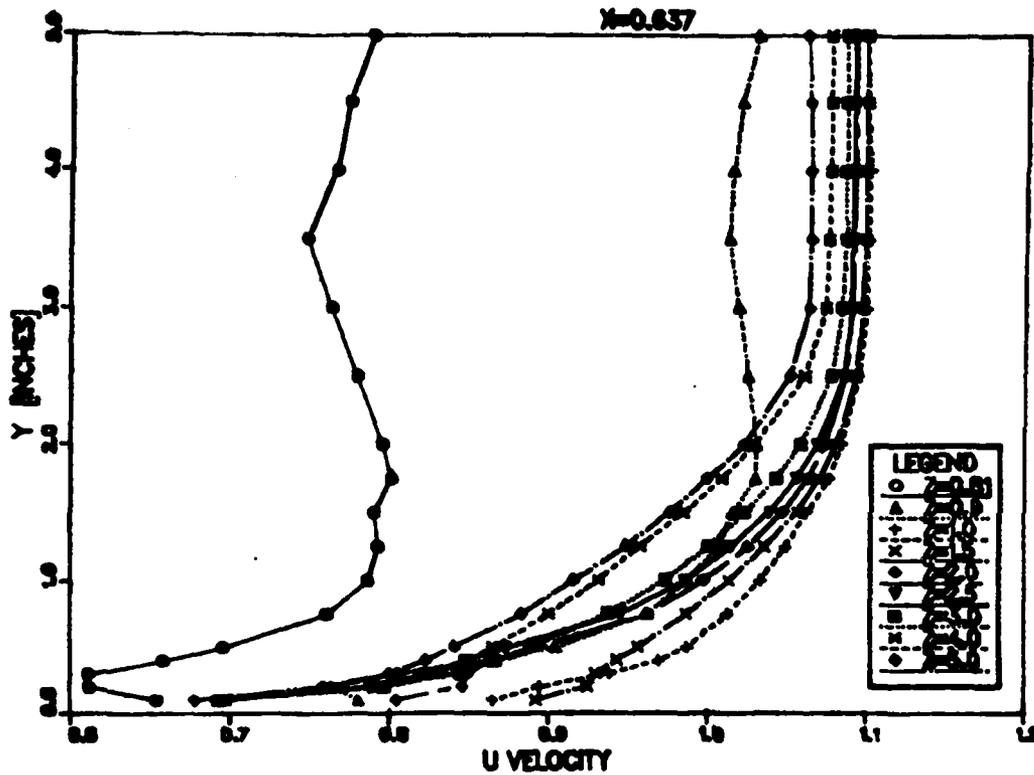**Fig. 24. Computed static pressure coefficients on the flat plate—elliptical nose.**

46

X=0.637

Fig. 25. u velocity profiles at x/c = 0.64, measured with
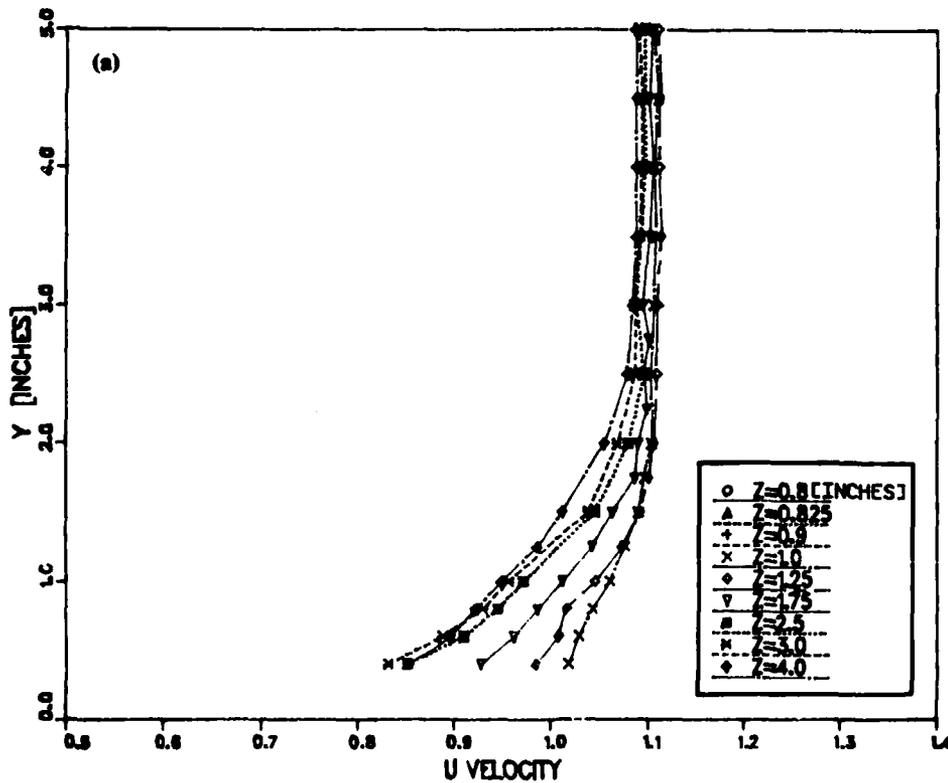hot-film anemometry—elliptical nose.

(a)

Fig. 26. u velocity profiles at x/c = 0.64, measured with laser doppler
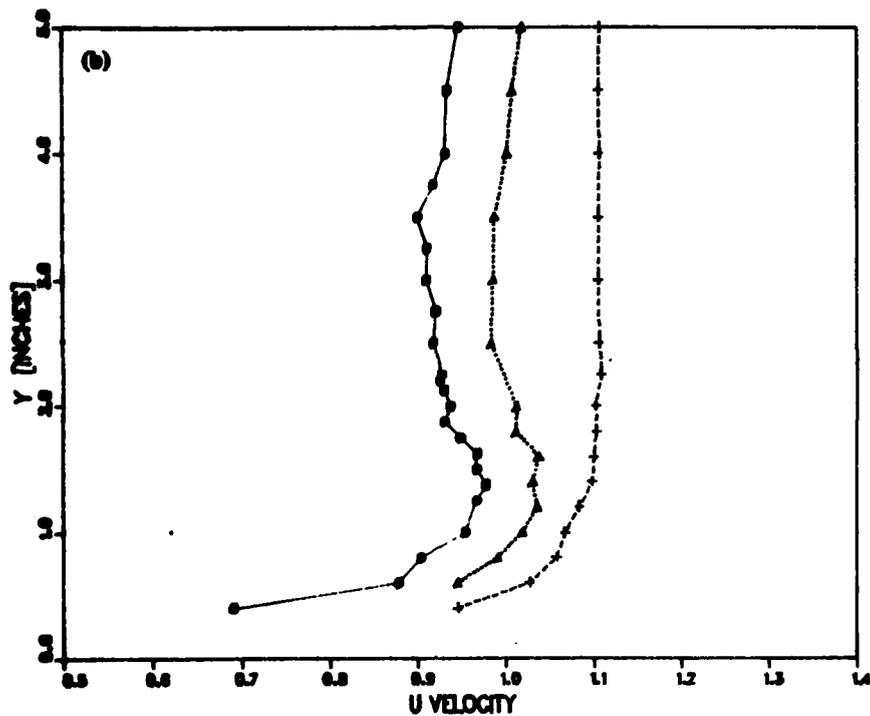anemometry—elliptical nose.

Fig. 26. (Continued)
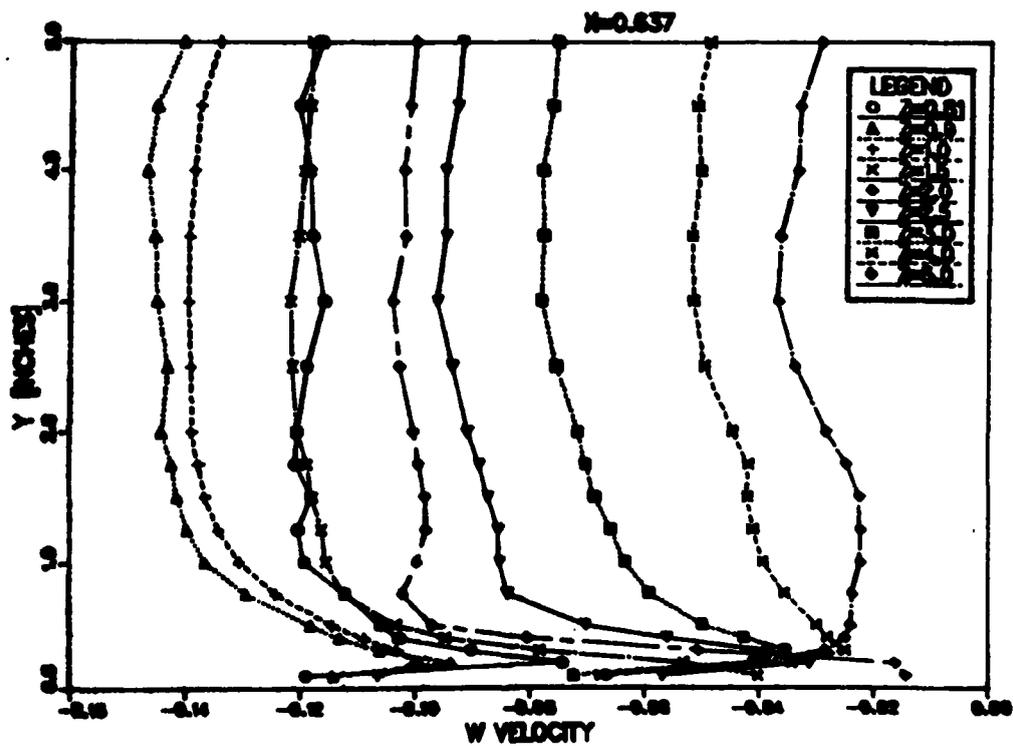

Fig. 27. w velocity profiles at x/c = 0.64, measured with
hot-film anemometry—elliptical nose.

48
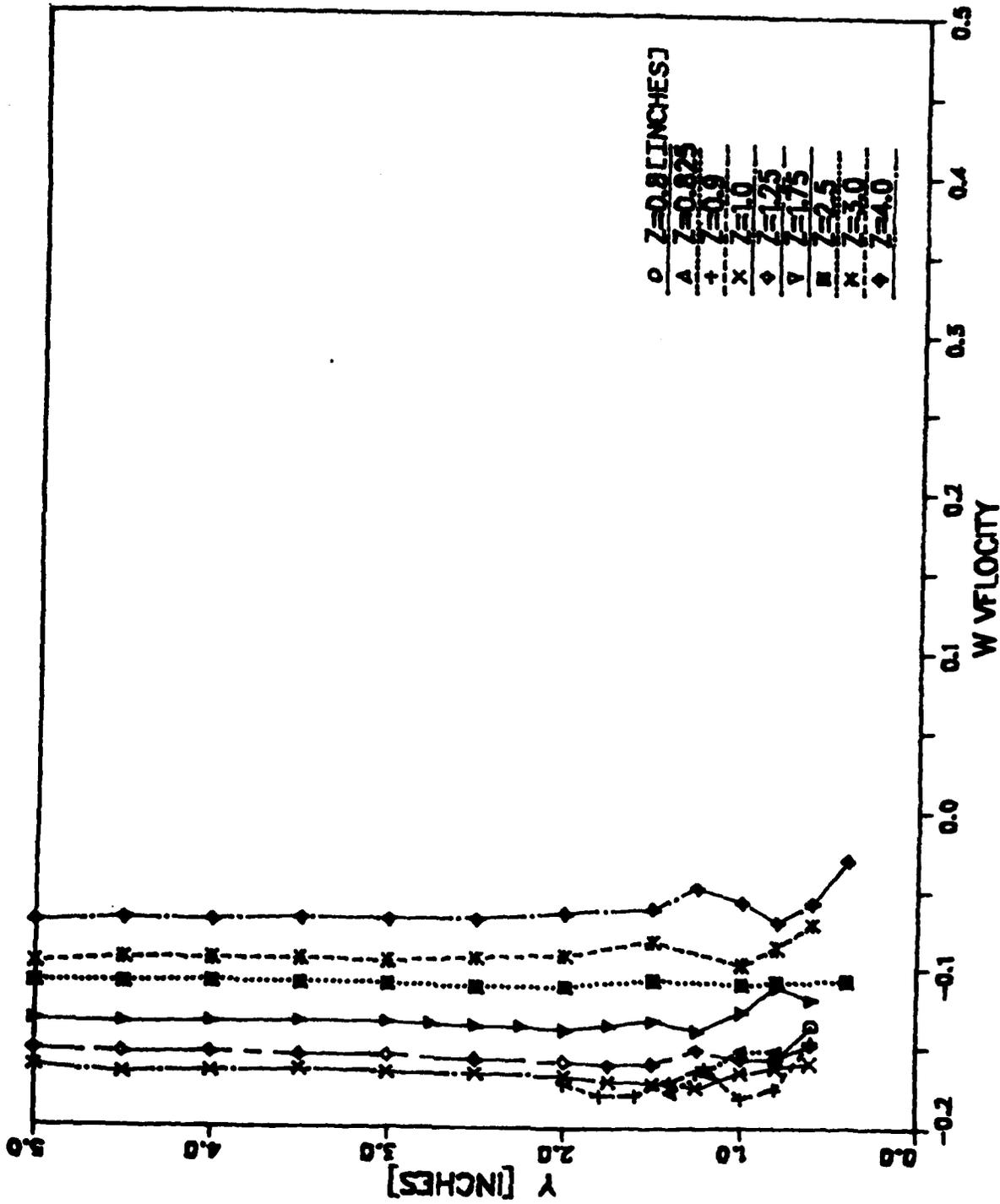
Fig. 28. w velocity profiles at x/c = 0.64, measured with laser dopper anemometry[17]—elliptical nose.

STREAMWISE VORTICITY CONTOURS
X/C = 0.18
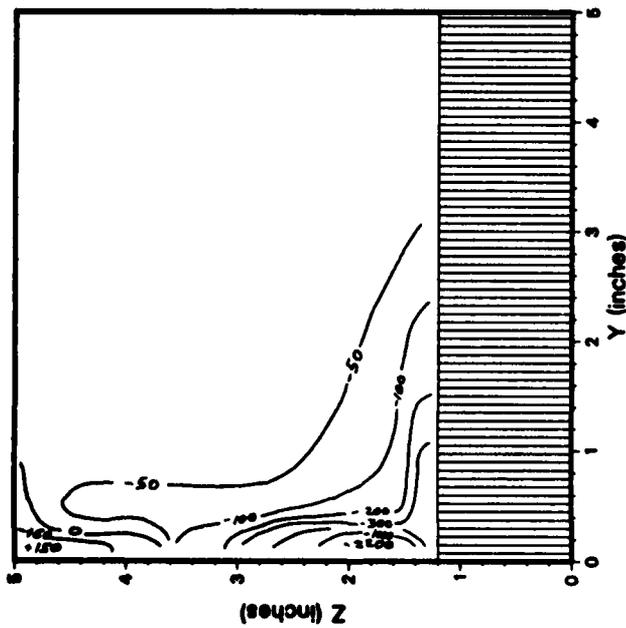
Fig. 29a. x/c = 0.18.

STREAMWISE VORTICITY CONTOURS
X/C = 0.64

Fig. 29b. x/c = 0.64.

Fig. 29. Streamwise vorticity contours—elliptical nose.

STREAMWISE VORTICITY CONTOURS

X/C = 0.93

Fig. 29d. x/c = 0.93.

STREAMWISE VORTICITY CONTOURS
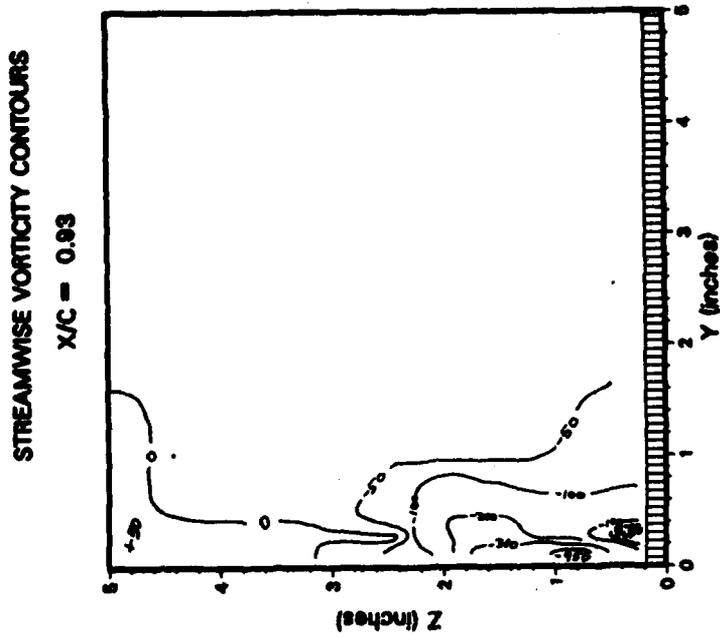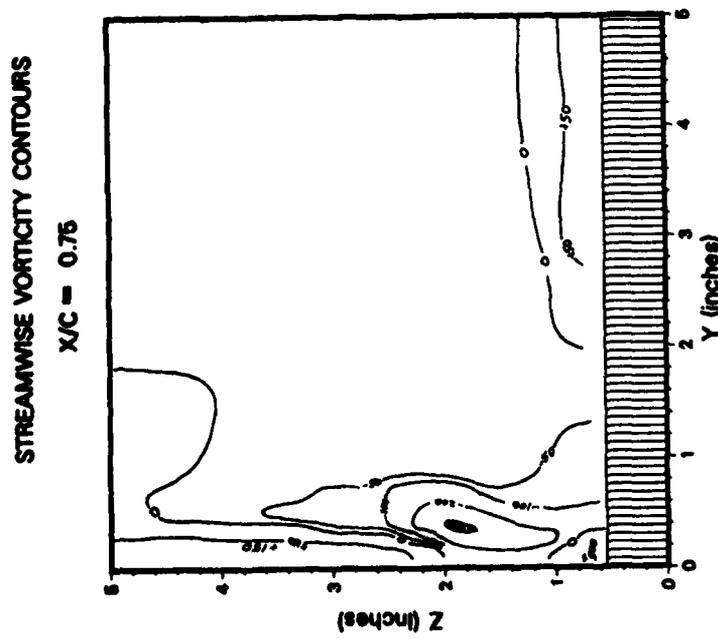
X/C = 0.75

Fig. 29c. x/c = 0.75.
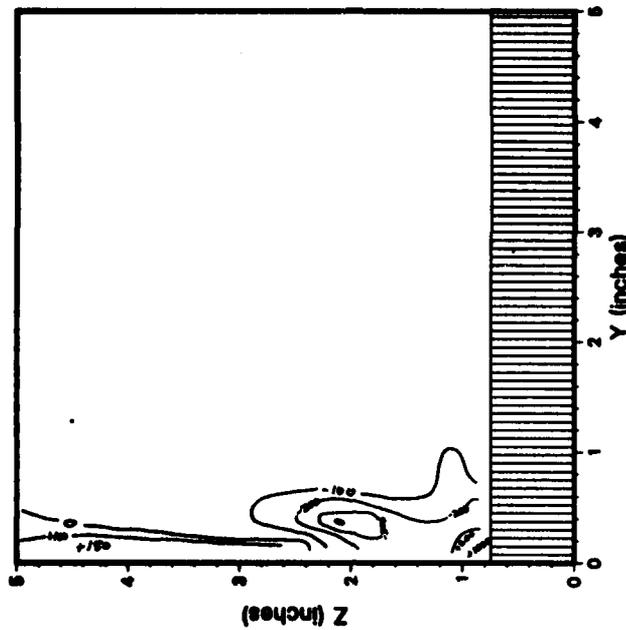
Fig. 29. (Continued)

51

STREAMWISE VORTICITY CONTOURS

X/C = 1.50

Z (inches)

Y (inches)
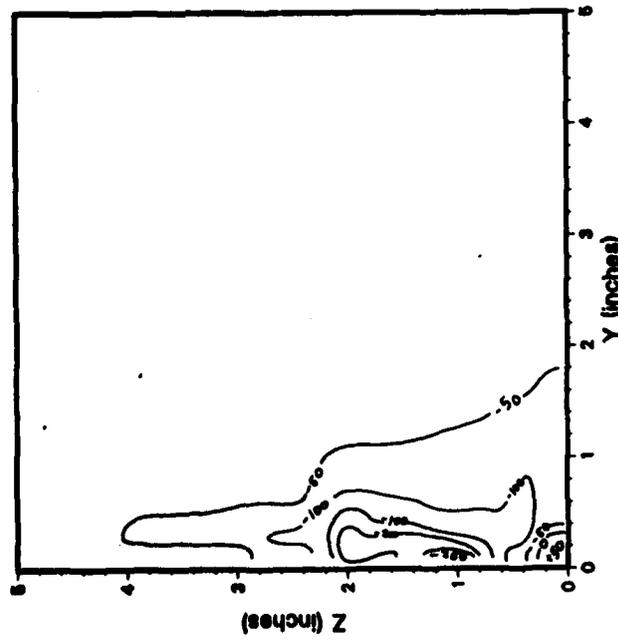
Fig. 29f. x/c = 1.50.

STREAMWISE VORTICITY CONTOURS

X/C = 1.05

Z (inches)

Y (inches)
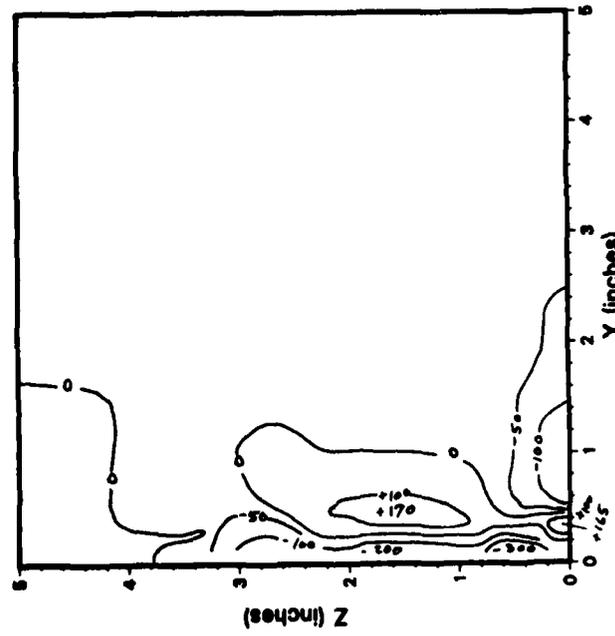
Fig. 29e. x/c = 1.05.

Fig. 29. (Continued)

52

Table 1. Offsets.

NACA 0020		Elliptical Nose Hybrid	
x	z	x	z
0.1500	0.2587	0.1500	0.4796
0.3000	0.5227	0.3000	0.6633
0.6000	0.7109	0.6000	0.8944
0.9000	0.8400	0.9000	1.0392
1.2000	0.9365	1.2000	1.1314
1.8000	1.0692	1.8000	1.2000
2.4000	1.1477	3.0000	1.1609
3.0000	1.1885	4.3000	1.0589
3.6000	1.2005	5.4000	0.9127
4.8000	1.1609	6.6000	0.7327
6.0000	1.0589	7.8000	0.5249
7.2000	0.9127	9.0000	0.2897
8.4000	0.7327	9.6000	0.1613
9.6000	0.5249	10.2000	0.0252
10.8000	0.2897		
11.4000	0.1613		
12.0000	0.0252		

REFERENCES

1. Peake, D.J. and M. Tobak, "Three-Dimensional Interactions and Vortical Flows with Emphasis on High Speed Flows," NATO AGARDograph No. 252 (Jul 1980).

2. Sung, C.H., "Numerical Wake Prediction Methods for Submerged Appended Bodies, A Literature Survey," DTNSRDC Report SPD-1057/01 (Feb 1983).

3. Love, R.H., "An Investigation of the Effect of the Wall Boundary Layer on the Wake of an Obstacle Protruding from the Wall," University of Maryland, Technical Note BM-370 (Aug 1963).

4. Belik, L., "The Secondary Flow about Circular Cylinders Mounted Normal to a Flat Plate," *Aeronautical Quarterly*, Vol. 26 (Feb 1973).

5. Baker, C.J., "The Turbulent Horseshoe Vortex," *Journal of Wind Engineering and Industrial Aerodynamics*, Vol. 6, Nos. 1-2 (Jul 1980).

6. Shabaka, I.M.M.A., "Turbulent Flow in an Idealized Wing-Body Junction," Ph.D. Thesis, Imperial College of Science and Technology (Apr 1969).

7. Shabaka, I.M.M.A. and P. Bradshaw, "Turbulent Flow Measurements in an Idealized Wing/Body Junction," *AIAA Journal*, 81-4028 (1981).

8. Oguz, E.A., "An Experimental Investigation of the Turbulent Flow in the Junction of a Flat Plate and a Body of Constant Thickness," Ph.D. Thesis, Georgia Institute of Technology (Dec 1980).

9. Kubendran, L.R., "Study of Turbulent Flow in a Wing-Fuselage Type Junction," Ph.D. Dissertation, Georgia Institute of Technology (Apr 1983).

10. McMahon, H., J. Hubbart, and L. Kubendran, "Mean Velocities and Reynolds Stresses in a Juncture Flow," NASA contractor Report 3605 (1982).

11. McMahon, H., J. Hubbart, and L. Kubendran, "Mean Velocities and Reynolds Stresses Upstream of a Simulated Wing-Fuselage Juncture," NASA contractor Report 3695 (Jun 1983).

12. Pierce, F.J. and J.E. McAllister, "Near Wall Similarity in a Pressure-Driven Three-Dimensional Turbulent Boundary Layer," Virginia Polytechnic Institute and State University Report VPI-E-80.32 (Sep 1980).

13. Pierce, F.J. and J.E. McAllister, "Measurements in a Pressure-Driven and a Shear-Driven Three-Dimensional Turbulent Boundary Layer," *Three-Dimensional Turbulent Boundary Layers*, H.H. Fernholz, and E. Krause editors, Springer-Verlag (1982).

14. Menna, J.D. and F.J. Pierce, "A Three-Dimensional Turbulent Boundary Layer Upstream and Around a Junction Vortex Flow," Virginia Polytechnic Institute and State University Report VPI-E-84-23 (Jun 1984).

15. Harsh, M.D. and F.J. Pierce, "An Experimental Investigation of a Turbulent Junction Vortex," Virginia Polytechnic Institute and State University Report VPI-E-85-4 (Feb 1985).

16. Pierce, F.J., M.D. Harsh, and J.D. Menna, "The Mean Flow Structure Around and Within a Turbulent Junction or Horseshoe Vortex," Virginia Polytechnic Institute and State University Report VPI-E-85-19 (Sep 1985).

17. Dickinson, S.C., "Flow Visualization and Velocity Measurements in the Separated Region of an Appendage-Flat Plate Junction," DTNSRDC Report 86/020 (Mar 1986).

18. Rood, E.P., "Experimental Investigation of the Turbulent Large Scale Temporal Flow in the Wing-Body Junction," Ph.D. Dissertation, The Catholic University of America (1984).

19. Rood, E.P. and J.E.C. Keller, "Evidence of Large Scale Time Dependent Flow in the Wing-Wall Interraction Wake," *Unsteady Turbulent Boundary Layers and Friction*, ASME Publication, FED Vol. 12 (1984).

20. Rood, E.P., "The Separate Spatial Extents of the Trailing Horseshoe Vortex Legs from a Wing and Plate Junction," *AIAA* 84-1526 (Jun 1984).

21. Rood, E.P., "The Governing Influence of the Nose Radius on the Unsteady Effects of Large Scale Flow Structure in the Turbulent Wing and Plate Junction Flow," *Forum On Unsteady Flow*, P.H. Rothe editor, ASME Publication, FED Vol. 15 (Dec 1984).

22. Rood, E.P. and D.G. Anthony, "Tail Profile Effects on Unsteady Large Scale Flow Structure in the Wing and Plate Junction," *Forum On Unsteady Flow*, P.H. Rothe editor, ASME Publication, FED Vol. 27 (1985).

23. Hasan, M.A.Z., M.J. Casarella, and E.P. Rood, "An Experimental Study of the Flow and Wall Pressure Field Around a Wing-Body Junction," *Shear Flow — Structure Interaction Phenomena*, A. Akay and M. Reischman editors, ASME Publication, NCA Vol. 1 (1985).

24. Lighthill, M.J., "Attachment and Separation in Three-Dimensional Flow," in *Laminar Boundary Layers*, Section II 2.6, L. Rosenhead editor, Oxford University Press (1963).

25. Hunt, J.C.R., C.J. Abell, J.A. Peterka, and H. Woo, "Kinematical Studies of the Flows around Free or Surface-mounted Obstacles; Applying Topology to Flow Visualization," *Journal of Fluid Mechanics*, Vol. 86, Part 1 (1978).

26. Perry, E. and H. Hornung, "Some Aspects of Three-Dimensional Separation, Part II: Vortex Skeletons," *Z. Flugwiss. Weltraumforsch*, 8, Heft 3 (1984).

27. Gorski, J.J., T.R. Govindan, and B. Lakshminarayana, "Computation of Three-Dimensional Turbulent Shear Flows in Corners," *AIAA Journal*, Vol. 23, No. 5 (May 1985).

28. *The 1980-81 AFSOR/HTTM Stanford Conference on Complex Turbulent Flows: A Comparison of Computation and Experiment*, Vols. I-III. Edited by S.J. Kline, B.J. Cantwell, and G.M. Lilley, Stanford University (1981).

29. Ilegbusi, J.O., "Numerical Calculation of Turbulent Corner Flows," *Applied Math Modeling*, Vol. 9 (Aug 1985).

30. Smith, F.T. and J. Gajjar, "Flow Past Wing-Body Junctions," *Journal of Fluid Mechanics*, Vol. 44 (1984).

31. Kaul, U.K., D. Kwak, and C. Wagner, "A Computational Study of Saddle Point Separation and Horseshoe Vortex System using the Three-Dimensional Incompressible Navier-Stokes Code," AIAA Paper, 85-0182 (Jan 1985).

32. Briley, W.R. and H. McDonald, "Computation of Three-Dimensional Horseshoe Vortex Flow using Navier Stokes Equations," *Seventh International Conference in Numerical Methods in Fluid Mechanics,* W.C. Reynolds and R.W. MacCormack editors, Springer-Verlag (1980).

33. Hung, C.M. and R.W. MacCormack, "Numerical Solution of Three-Dimensional Shock Wave and Turbulent Boundary Layer Interaction," *AIAA Journal,* Vol. 16, No. 10 (1978).

34. Hung, C.M. and P.G. Buning, "Simulation of Blunt-Fin-Induced Shock-Wave and Turbulent Boundary-Layer Interaction," *Journal of Fluid Mechanics,* Vol. 154 (1985).

35. Baldwin, B.S. and H. Lomax, "Thin Layer Approximation and Algebraic Model for Separated Turbulent Flows," AIAA Paper 78-257 (Jan 1978).

36. Scottron, V.E. and D.A. Shaffer, "The Low-Turbulence Wind Tunnel," DTMB Report 2116 (Dec 1965).

37. Middlekauff, R.D. and S.C. Dickinson, "A General Hotwire Data Collection Program: Documentation and Users Manual," DTNSRDC Report SPD-1157/01 (Aug 1985).

38. Langston, L.S. and M.T. Boyle, "A New Surface-Streamline Flow-Visualization Technique," *Journal of Fluid Mechanics,* Vol. 125 (Dec 1982).

39. Chang, M.S. and Y.T. Shen, "Computer Programs, 'Hydrofoil and Airfoil' for calculation of Potential Flow About Two-Dimensional Foils," DTNSRDC Report SPD-1037/01 (Aug 1982).

INITIAL DISTRIBUTION

Copies

3 CONR
  1 1132F J. Fein
  1 1132F M. Reischman
  1 1245 R. Hansen

3 NAVSEA
  1 SEA 55W33 E. Comstock
  1 SEA 55W31 W. Sandberg
  1 SEA 55W31 G. Jones

2 NRL
  1 Code 2027
  1 Code 2629

2 NBS
  1 Klebanoff
  1 Lib

2 NASA, Langley
  1 Kubendran
  1 Lib

2 NASA, Ames
  1 Kwak
  1 Lib

12 DTIC

2 Flow Research Co.
  1 Duncan
  1 Gad-el-Hack

2 Gould Defense Systems, Inc.
  1 Meng
  1 Dickinson

1 Massachusetts Institute of Tech.
    Merrill

1 Univ. of Southern California
    Ho

Copies

4 Virginia Poly. Inst. & State Univ.
  1 Pierce
  1 Moore
  1 Shetz
  1 Simpson

2 Georgia Institute of Tech.
  1 Hubbartt
  1 McMahon

4 Pennsylvania State Univ.
  1 Merkle
  1 Parkin
  1 Hoffman
  1 ARL-Lib

1 Univ. of Southern California
    Eibeck

1 Rutgers Univ.
    Knight

2 Univ. of Iowa
  1 Patel
  1 Stern

5 Stevens Institute of Tech.
  1 Speziale
  1 Savitsky
  1 Breslin
  1 McKee
  1 DL-Lib

1 New Jersey Institute of Tech.
    Battifarano

3 Scientific Research Assoc., Inc.
  1 Levy
  1 Shamroth
  1 Briley

1 Lockheed Georgia Co.
    Thomas

1 Lockheed Missile and Space Co.
    Burke

CENTER DISTRIBUTION

Copies	Code	Name
1	012.2	Nakonechney
1	15	Morgan
1	1504	Monacella
1	152	Lin
1	1522	Sung
1	154	McCarthy
1	1542	Huang
25	1542	Hendrix
1	1543	Rood
1	1543	Anthony
1	1544	Peterson
1	1544	Reed
1	1843	Haussling
10	5211.1	Reports Control
1	522.1	TIC (C)
1	522.2	TIC (A)

DTNSRDC ISSUES THREE TYPES OF REPORTS:

1. **DTNSRDC reports, a formal series,** contain information of permanent technical value. They carry a consecutive numerical identification regardless of their classification or the originating department.

2. **Departmental reports, a semiformal series,** contain information of a preliminary, temporary, or proprietary nature or of limited interest or significance. They carry a departmental alphanumerical identification.

3. **Technical memoranda, an informal series,** contain technical documentation of limited use and interest. They are primarily working papers intended for internal use. They carry an identifying number which indicates their type and the numerical code of the originating department. Any distribution outside DTNSRDC must be approved by the head of the originating department on a case-by-case basis.

END

7-87

DTIC